The ionization parameter of star-forming galaxies evolves with the specific star formation rate

Melanie Kaasinen,[1,2,3]★ Lisa Kewley,[1,4] Fuyan Bian,[1]† Brent Groves,[1,4]
Daichi Kashino,[5] John Silverman[6] and Jeyhan Kartaltepe[7]

[1]*Research School of Astronomy and Astrophysics, Australian National University, Weston Creek 2611, Australia*
[2]*Max-Planck-Institut für Astronomie, Königstuhl 17, D-69117 Heidelberg, Germany*
[3]*Universität Heidelberg, Zentrum für Astronomie, Institut für Theoretische Astrophysik, Albert-Ueberle-Straße 2, D-69120 Heidelberg, Germany*
[4]*ARC Centre of Excellence for All Sky Astrophysics in 3 Dimensions (ASTRO 3D)*
[5]*Department of Physics, ETH Zürich, Wolfgang-Pauli-Strasse 27, CH-8093 Zürich, Switzerland*
[6]*Kavli Institute for the Physics and Mathematics of the Universe, The University of Tokyo, Kashiwa 277-8583 (Kavli IPMU, WPI), Japan*
[7]*School of Physics and Astronomy, Rochester Institute of Technology, 84 Lomb Memorial Drive, Rochester, NY 14623, USA*

ABSTRACT

We investigate the evolution of the ionization parameter of star-forming galaxies using a high-redshift ($z\sim 1.5$) sample from the FMOS-COSMOS (Fibre Multi-Object Spectrograph-COSMic evOlution Survey) and matched low-redshift samples from the Sloan Digital Sky Survey. By constructing samples of low-redshift galaxies for which the stellar mass (M_*), star formation rate (SFR), and specific star formation rate (sSFR) are matched to the high-redshift sample, we remove the effects of an evolution in these properties. We also account for the effect of metallicity by jointly constraining the metallicity and ionization parameter of each sample. We find an evolution in the ionization parameter for main-sequence, star-forming galaxies and show that this evolution is driven by the evolution of sSFR. By analysing the matched samples as well as a larger sample of $z< 0.3$, star-forming galaxies we show that high ionization parameters are directly linked to high sSFRs and are not simply the by-product of an evolution in metallicity. Our results are physically consistent with the definition of the ionization parameter, a measure of the hydrogen ionizing photon flux relative to the number density of hydrogen atoms.

Key words: galaxies: evolution – galaxies: high-redshift – galaxies: ISM.

1 INTRODUCTION

Most high-redshift ($z> 1$) star-forming galaxies appear to have significantly different properties to the dominant population of local star-forming galaxies. High-redshift (high-z) star-forming galaxies typically have 10–100 times higher star formation rates (SFRs; Daddi et al. 2007; Elbaz et al. 2011; Speagle et al. 2014), 3−10 times higher gas fractions (Genzel et al. 2008; Tacconi et al. 2010), and higher gas velocity dispersions (Erb et al. 2006; Förster Schreiber et al. 2006; Daddi et al. 2007; Genzel et al. 2008; Tacconi et al. 2010) than local star-forming galaxies of the same stellar mass (M_*). High-z galaxies also appear to be smaller by 0.3−0.5 dex (Trujillo et al. 2007; van der Wel et al. 2014) and more 'clumpy' (e.g. Elmegreen & Elmegreen 2005) than local star-forming galaxies.

The differences between local and high-z star-forming galaxies are largely driven by the conditions within the inter-stellar medium (ISM). The most convenient way to probe the ISM conditions of both local and high-redshift star-forming galaxies is to study their rest-frame optical emission. This emission is typically dominated by a small set of strong emission lines, consisting of hydrogen recombination lines and collisionally excited metal lines, which stem from regions of the ISM that have been ionized by recent (<5 Myr) star formation. The relative strengths of these strong emission lines reflect the ionizing sources and physical conditions of the ionized ISM, particularly of the most luminous H ɪɪ regions.

Over the last decade, large samples of high-redshift, star-forming galaxies with rest-frame optical emission-line measurements have been assembled (e.g. Masters et al. 2014; Shapley et al. 2015; Silverman et al. 2015). The ensuing studies have found that high-redshift star-forming galaxies exhibit emission-line ratios that are atypical of the local star-forming galaxy population (e.g. Hainline et al. 2009; Kewley et al. 2013a; Steidel et al. 2014; Hayashi et al.

★ E-mail: kaasinen@mpia.de
† Stromlo Fellow.

2015; Shapley et al. 2015). In particular, there is increasing evidence for an enhancement of the [O III]λλ4959, 5007/[O II]λλ3726, 3729, and [O III]λ5007/H β ratios with respect to local galaxies. These elevated emission-line ratios indicate that at least some ISM conditions must have evolved since the early Universe. But it is still unclear which ISM conditions are evolving and to what extent.

The conditions within the ionized ISM can be described by a small set of physical properties including the metallicity, ionization parameter, pressure, and hardness of the ionizing radiation field (e.g. Dopita et al. 2006b; Dopita et al. 2013; Kewley et al. 2013b; Vogt et al. 2014). The gas-phase metallicity of typical, high-z, star-forming galaxies is lower in the local population (e.g. Erb et al. 2006; Liu et al. 2008; Zahid et al. 2013). However, the evolution of metallicity alone is not sufficient to account for the elevated [O III]λλ4959, 5007/[O II]λλ3726, 3729 and [O III]λ5007/H β ratios at high redshift (e.g. Kewley et al. 2013a; Masters et al. 2014; Shirazi, Brinchmann & Rahmati 2014b; Steidel et al. 2014). Other ISM conditions that may account for the observed changes include higher ionization parameters and/or electron densities (e.g. Brinchmann, Pettini & Charlot 2008; Kewley et al. 2013b; Shirazi et al. 2014b; Steidel et al. 2014; Kewley et al. 2015), harder ionizing radiation fields (Kewley et al. 2013b; Steidel et al. 2014), contributions from shocks/active galactic nucleus (AGN; Groves, Heckman & Kauffmann 2006; Newman et al. 2014) and a variation in N/O ratio (e.g. Shapley et al. 2015; Masters, Faisst & Capak 2016).

Many studies find evidence for increased ionization parameters at high redshift (e.g. Hainline et al. 2009; Bian et al. 2010; Masters et al. 2014; Shirazi et al. 2014a,b; Sanders et al. 2016). The ionization parameter, q, is a measure of the current star formation distribution and ionization state of the ISM, reflecting the interaction between the ionizing source and ionized gas. Defined as the ratio between the mean hydrogen ionizing photon flux and the density of hydrogen atoms (e.g. Dopita & Sutherland 2003; Osterbrock & Ferland 2006), the ionization parameter increases with the luminosity of the stellar population and the hardness of the ionizing radiation field.

Although there is a range of physical mechanisms that can increase the ionization parameter of H II regions, it is still unclear what is driving the high ionization parameters of high-z, star-forming galaxies. High-redshift studies have often been limited by small sample sizes with insufficient emission lines that are sensitive to the ionization parameter, relying on the use of a single emission-line ratio as a proxy for the ionization parameter. Nakajima & Ouchi (2014) suggest that the high inferred ionization parameters at high redshift are the by-product of lower metallicities, but the inverse correlation between the ionization parameter and metallicity of H II regions (Dopita et al. 2006b) has not yet been demonstrated on a global scale. It has also been suggested that high ionization parameters are the result of high SFRs, which lead to a larger reservoir of ionizing photons (e.g. Hainline et al. 2009; Kewley et al. 2013b). Although many of the galaxies with high ionization parameters have high SFRs, both locally and at high redshift, there is still no direct evidence for an increase in ionization parameter with SFR.

Previous observational studies have struggled to disentangle the evolution of the ionization parameter from both selection effects and the evolution of global galaxy properties. High-redshift studies typically sample galaxies with intrinsically luminous emission lines (Calvi et al. 2014; Juneau et al. 2014), such as starburst galaxies or galaxies containing significant contributions from shocks or AGN (Groves et al. 2006; Trump et al. 2011), which have higher ionization parameters. Moreover, most high-redshift spectroscopic surveys are targeted at the dominant population of star-forming

galaxies, i.e. main-sequence galaxies (at 10^9–10^{11} M$_\odot$), which are offset to higher SFRs and sSFRs at high redshift (Madau & Dickinson 2014; Speagle et al. 2014). Although previous studies have provided evidence for a correlation between global galaxy properties (i.e. M_* and SFR) and the gas-phase metallicity (e.g. Tremonti et al. 2004; Mannucci et al. 2010; Zahid et al. 2014a), the relationship with ionization parameter remains unclear.

Recent studies indicate that the elevated [O III]λλ4959, 5007/[O II]3726, 3729 and [O III]λ5007/H β ratios and high inferred values of electron density and ionization parameter are related to higher specific star-formation rates (sSFR; SFR/M) (Kewley et al. 2015; ${}_*$Bian et al. 2016; Holden et al. 2016). Bian et al. (2016) find that local galaxies with the elevated [O III]/H β ratios typical of galaxies at $z\sim 2$ have significantly higher electron densities, ionization parameters, and sSFRs. Conversely, Dickey et al. (2016) show that high-redshift galaxies with low sSFRs (log (sSFR/ yr^{-1}) < −9) also exhibit low [O III]/H β ratios (log([O III]/H β) < 0.3).

Although these studies go some way to linking global properties with ISM conditions, they do not isolate the impact that global properties such as the SFR and sSFR have on the ionization parameter. We investigate the extent to which the M_*, SFR, and sSFR impact the evolution of the ionization parameter by comparing samples of low- and high-z galaxies matched in these properties. By matching samples we remove the effects of the evolution of M_*, SFR, or sSFR with redshift. We account for the evolution of metallicity and the degeneracy between strong emission-line ratios and different ISM properties by applying diagnostic methods which simultaneously infer the metallicity and ionization parameter.

This paper is structured as follows. In Section 2, we describe the main high-z sample and the matched low-z comparison samples. We describe the observations, data reduction, and relative aperture correction factors for our main high-z ($z \sim 1.5$) sample in Section 3. In Section 4, we describe the methods used to derive stacked emission-line fluxes for our samples. We outline the methods used to diagnose the ionization parameter and metallicity in Section 5. We present our results, including the emission-line properties, metallicities, and ionization parameters in Section 6. In Section 7, we discuss the validity of our methods and the relationships between the ionization parameter, metallicity, and global galaxy properties. Finally, in Section 8, we summarize our findings.

Throughout this paper, we refer to values of SFR, sSFR, and M_* consistent with a Kroupa IMF. We select the Kroupa IMF for consistency with the SFRs of the Sloan Digital Sky Survey (SDSS) sample. We adopt a Λ-CDM cosmology with $H_0 = 70$ km s^{-1} Mpc^{-1}, $\Omega_m = 0.3$, and $\Omega_\Lambda = 0.7$. Throughout the paper, we use 'metallicity' and Z to mean the gas-phase oxygen abundance relative to hydrogen, $12 + \log (O/H)$.

2 SAMPLE SELECTION

2.1 High-z sample

To investigate the evolution of the ionization parameter, we assemble a sample of star-forming galaxies at $z \sim 1.5$ with rest-frame optical emission-line flux measurements of [O II]λλ3726, 3729, H β, [O III]λ5007, H α, and [N II]λ6584. Our sample is derived from two spectroscopic surveys of star-forming galaxies in the COSMic evOlution Survey (COSMOS) field. The initial survey, undertaken with the Fibre Multi-Object Spectrograph (FMOS) on Subaru (P.I.s Sanders and Silverman; Silverman et al. 2015), yielded detections

of Hβ, [O III]λ5007, Hα, and,[N II]λ6584, whereas the complementary survey undertaken with the DEep Imaging Multi-Object Spectrograph (DEIMOS) on Keck II (P.I. Kewley; Kaasinen et al. 2017) provided observations of the [O II] doublet. We investigated the evolution of the electron density using the COSMOS-[O II] sample in Kaasinen et al. (2017), showing that the electron density does not evolve with redshift when the changing SFR is taken into account. In this work, we investigate the evolution of the ionization parameter and its dependence on M_*, SFR, and sSFR.

Both spectroscopic surveys were targeted at massive ($>10^{9.8}$ M$_\odot$), star-forming galaxies at $1.4 < z < 1.8$, identified from the COSMOS photometric catalogues (McCracken et al. 2012; Ilbert et al. 2013). Initial stellar masses and photometric redshifts for target selection were estimated via the broad-band photometry and fitting results of LePHARE (Arnouts & Ilbert 2011), using Bruzual & Charlot (2003) population synthesis models and a Chabrier IMF. FMOS-COSMOS targets were selected to have a photometric redshift within the optimal range for the H-long or H-short grating ($R \sim 3000$; 1.6–1.8 µm, 1.4–1.6µm) and a Hα flux above the required threshold for detectability (see Silverman et al. 2015 for details). Galaxies with Hα detections were re-observed using the J-long grating ($R \sim 2200$; 1.11–1.35 µm) to detect Hβ and [O III]λ5007. Follow-up *J*-long observations were prioritized based on the reliability of the spectroscopic redshifts. The complementary COSMOS-[O II] survey targeted ~800 galaxies with SFR$_{phot}$ > 10 M$_\odot$ yr^{-1} and z(AB) magnitudes $\lesssim$24 (SuprimeCam, z^{++}, $\lambda_c = 9106$, Laigle et al. 2016). To minimize AGN contamination, galaxies with X-ray detections were excluded from the COSMOS-[O II] Survey.

To reliably probe the relative strengths of the five strong emission lines used in this study, [O II]λ3727, Hβ, [O III]λ5007, Hα, and [N II]λ6584, we require observations in all three wavelength regimes. Of the ~380 galaxies with FMOS *H*- and *J*-band observations, 97 have corresponding DEIMOS observations. We discard 12 galaxies with DEIMOS spectra that do not cover the predicted wavelength of the [O II]λ3726, 3729 doublet or for which the spectrum is impacted by issues such as sky continuum errors caused by scattered light from a neighbouring slit (see Newman et al. 2013). Of the remaining set, we remove three galaxies for which the [O III]/Hβ and [N II]/Hα ratios indicate the presence of an AGN based on the maximum starburst criteria of Kewley et al. (2001). Measurements of all five SELs used in this study are only available for 13 of the remaining 82 galaxies.

To increase the signal-to-noise ratio (S/N) of the strong emission line fluxes and allow for robust metallicity and ionization parameter determinations we rely on a stacked analysis (see Section 4). Constructing stacked spectra requires reliable spectroscopic redshift estimates. We therefore require at least two emission lines, detected at a S/N > 3, to confirm the spectroscopic redshift (to within Δz< 0.005). In all cases, we require the presence of Hα to confirm the redshift estimate. We remove 11 galaxies that do not meet these S/N constraints from our sample. We also exclude three galaxies which lie well below the star-forming main sequence at $z \sim 1.5$ (shaded pink region of Fig. 1) because our stacked analysis is aiming to probe properties that are representative of the dominant population of star-forming galaxies at $z \sim 1.5$. To reliably measure the Balmer decrement, Hα/Hβ, and metallicity based on stacked data, we remove a further 18 galaxies for which the Hβ or [O III]λ5007 lines are completely masked by a skyline. We refer to the final sample of 50 galaxies as the 'high-z sample'.

We rely on a combination of photometry and spectroscopy to derive the global properties referred to throughout this work. The stel-
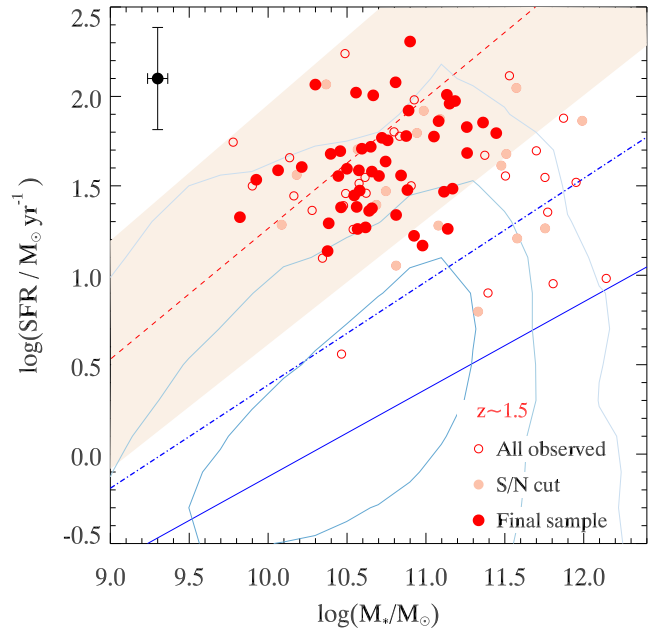
Figure 1. SFR versus M_* for the 'SDSS star-forming catalogue' (blue) and the $z \sim 1.5$ main and parent samples. Open red circles denote the initial sample of $z \sim 1.5$ galaxies with FMOS *H* and *J* bands and DEIMOS observations, not included in the final sample. The small filled pink circles show the subset of $z\sim 1.5$ galaxies with two lines detected at S/N > 3 and the final sample, the 'high-z sample' is shown by the filled red circles. The mean errors on the $z \sim 1.5$ data are indicated by the black error bars at the top left. Regions of M_* and SFR containing 67, 95, and 99 per cent of the low-z star-forming catalogue from which the matched samples are drawn are indicated by the blue contours. The solid blue, dashed blue, and dashed red lines represent the 'best, mixed' main-sequence fits at z= 0, 0.3, and 1.5, respectively, derived by Speagle et al. (2014). The pink filled region indicates the uncertainty the main-sequence fit at $z = 1.5$, based on the errors on the fitting coefficients derived by Speagle et al. (2014). Note that the high-z data represented by the three filled red circles just below the Speagle fit have been included in the final sample, as the SFR and M_* still consistent with the main sequence within the uncertainties.

lar masses of the high-z sample are taken from the latest COSMOS photometric catalogue (Laigle et al. 2016). These stellar masses are derived by fitting model spectra to the spectral energy distributions via LePHARE (Arnouts & Ilbert 2011) following the methods outlined by Ilbert et al. (2015). To convert the stellar masses to a Kroupa IMF, we apply a constant scaling factor of 1.06 (Zahid et al. 2012). The SFRs (and sSFRs) of our $z \sim 1.5$ sample were estimated from the dust-corrected Hα luminosities using the conversions in Murphy et al. (2011) and Hao et al. (2011) (consistent with a Kroupa IMF).

We compare the M_* and SFR of the high-z sample to both the full sample of galaxies observed with FMOS and DEIMOS and the sample for which two lines are detected at S/N > 3 in Fig. 1. The final high-z sample (filled red circles) is consistent with the larger parent sample (open and small pink circles) but restricted to a narrower M_* and SFR range and limited to the star-forming main-sequence at $z\sim 1.5$ by selection. As in previous high-redshift studies (e.g. Masters et al. 2014; Shapley et al. 2015; Sanders et al. 2016), our sample exhibits significantly higher SFRs and sSFRs than the dominant population of local ($z < 0.1$) star-forming galaxies (solid blue line) although there is significant scatter in the M_* versus SFR relation.

2.2 Low-z comparison samples

We derive our low redshift (low-z) comparison samples from the SDSS (York et al. 2000) Data Release 7 (DR7; Abazajian et al. 2009) catalogue. We use the emission-line measurements and SFRs from the MPA-JHU catalogues (Kauffmann et al. 2003; Brinchmann et al. 2004; Tremonti et al. 2004). Like the high-z sample, SDSS SFRs are estimated from the H α luminosities after correcting for aperture loss of the SDSS fibres and dust extinction based on H α/H β, and are based on a Kroupa IMF. In order to perform a fair comparison with the high-z sample, we adopt the stellar masses derived by Zahid et al. (2013) using LePhare. Stellar masses derived using LePhare are $\sim$0.2 dex lower on average than those from the MPA-JHU catalogue, with a $\sim$0.2 dex dispersion Zahid et al. (2013). As for our FMOS sample, we normalize the SDSS stellar masses to a Kroupa IMF, such that the IMFs used for the SFR and M_* are consistent. We note that our choice of LePhare stellar masses yields results in a mass–metallicity (MZ) relation consistent with Zahid et al. (2013) and that different sources of M_* and sSFR may impact the slope and turnover of the derived MZ relation.

To construct the catalogue from which we select our low-z comparison samples, we apply further constraints. We discard galaxies for which the M_* or SFR are not constrained (i.e. negative or infinite value). To individually determine the metallicity and ionization parameter and investigate the extent of AGN contamination, we enforce an S/N constraint of S/N > 3 on [O II]λ3727, H β, H α, and [N II]λ6584. However, we apply no S/N constraint on [O III]λ5007, to avoid biasing the average metallicities of galaxies with high stellar mass (Foster et al. 2012) and allow for a comparison with previous studies (e.g. Zahid et al. 2013). To reduce systematic errors from aperture effects, we select galaxies at $z > 0.04$ (Kewley, Jansen & Geller 2005).

We reject AGN based on the standard optical line ratios as for the high-z sample, by applying the Kewley et al. (2001) maximum starburst criteria. The Kewley et al. (2001) criteria places a theoretical upper limit on the location of star-forming galaxies beyond which the [O III]/H β and [N II]/H α ratios can no longer be modelled without the contribution of an AGN. As discussed by Kauffmann et al. (2003), the application of the Kewley et al. (2001) criteria to local galaxies may underestimate the contribution of AGN. We ensure that our choice of AGN cut-off had no impact upon our conclusions, by repeating our analysis using the upper limit of Kauffmann et al. (2003), which represents the maximum position of local star-forming galaxies on the BPT diagram.

We select four 'matched' SDSS comparison samples from the 'low-z star-forming catalogue', in order to study the evolution of ISM properties. These samples are matched to our high-z sample according to a different combination of global properties as follows:

   (i) M_*-matched: matched only in M_*,
   (ii) SFR-matched: matched only in SFR,
   (iii) sSFR-matched: matched only in sSFR, and
   (iv) M_*-and-SFR-matched: matched in both M_* and SFR.

To capture a sufficient sample of low-z galaxies with SFRs (and M_*) equivalent to those of the high-z sample (>10 each), we employ an upper redshift cut-off of $z< 0.3$. We refer to the sample of 224 892, star-forming low-z ($0.04 < z< 0.3$) SDSS galaxies from which we draw our comparison samples as the 'low-z star-forming catalogue'. The distribution of M_* and SFR for the low-z star-forming catalogue are indicated by blue contours in Fig. 1, which contain 67, 95, and 99 per cent of the sample. We recover an evolution in the main sequence from the low-z star-forming catalogue to the high-z

sample (red filled circles) and show that the majority of $z< 0.3$ star-forming galaxies encompass the same stellar mass range as the high-z sample, but typically have lower SFRs.

Each 'matched' low-z sample is created by randomly selecting an ensemble of $z< 0.3$ counterparts for every high-z galaxy. To ensure that the distribution of the global property being matched is the same for the low- and high-z samples, we select the same number of low-z counterparts for each high-z galaxy. We limit the M_*- and sSFR-matched samples to 100 low-z counterparts per high-z galaxy to minimize the computational cost. Further increases in the size of these matched ensembles had no impact upon the mean or spread in the emission-line properties of the stacked samples. For the two samples matched in SFR, the size of the matched ensembles is determined by the minimum possible number of matches to galaxies in the high-z sample. Because we find only 37 low-z galaxies, with equivalent SFRs to the highest SFR galaxy in the high-z sample, we select 37 counterparts for each of the galaxies in the high-z sample. Similarly, we select only 10 counterparts in M_* and SFR, per high-z galaxy, to construct the M_*-and-SFR-matched sample.

The tolerances used for matching are selected based on the mean errors on the high-z sample. We create the M_*-matched sample by selecting galaxies for which the M_* is consistent to within 0.1 dex with the M_* of the high-z counterpart and create the SFR-matched sample by selecting low-z galaxies for which the SFR is consistent to within 0.2 dex that of each high-z galaxy. To create the sSFR-matched sample, we select galaxies for which the sSFR is consistent to within 0.15 dex that of the high-z galaxy. Only the ratio of SFR to M_* is equivalent to the high-z counterparts, not the values of M_* or SFR (see the third row of Fig. 2). For our final sample, we select local counterparts for which both the M_* and SFR are consistent to within $\sim$0.2 dex.

We compare the distributions of M_*, SFR, and sSFR of our low-z matched samples to the high-z sample in Fig. 2. Because of the evolution of the main sequence and the sample characteristics of SDSS, the majority of M_*-matched, low-z galaxies have both lower SFRs and sSFRs than the high-z sample (the top row of Fig. 2). Conversely, the majority of SFR-matched low-z galaxies have higher M_* and lower sSFRs. Most sSFR-matched local galaxies have both lower M_* and SFRs than the high-z sample.

3 HIGH-z DATA

3.1 Observations and data reduction

Our sample of $z \sim 1.5$ galaxies is based on three sets of observations, two from FMOS (*H* and *J* bands) and one with DEIMOS. The H-long and *H*-short observations were conducted over fourteen nights in 2012 March, 2013 January, 2013 December, 2014 January, and 2014 February with follow-up *J*-band observations conducted over six nights in 2012 March, 2013 January, and 2014 February. The average seeing for the FMOS observations was $\sim$1.0 arcsec, although it varied significantly over these six nights. Approximately 940 galaxies at $z \sim 1.5$ were observed in the *H* band, with a subset of $\sim$380 observed in the *J* band.

The corresponding DEIMOS observations were conducted over two clear nights, UTC 2014 February 24 and 25. All DEIMOS observations were conducted with the 600ZD grating centred at 7500Å, the OG550 filter and 1 arcsec slit width. The average seeing over the two nights of the DEIMOS observations was $\sim$0.75 arcsec. Approximately 430 galaxies at $1.4 <z < 1.7$ were observed with DEIMOS over the course of the two nights. The FMOS and
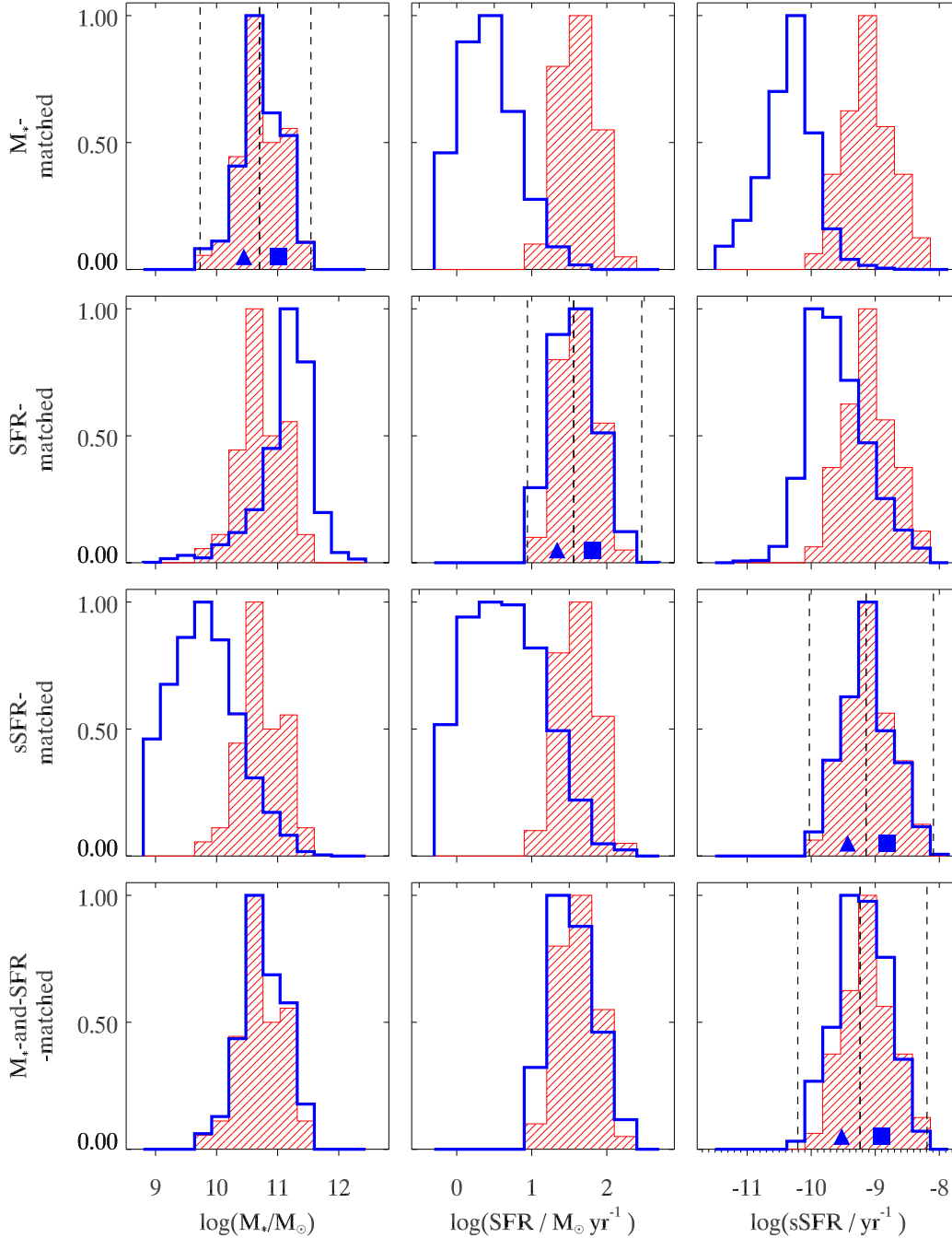
Figure 2. Distribution of global properties for the high-*z* (red line fill) versus low-*z* matched (blue outline) samples. The left, middle, and right-hand columns show the distribution of M_*, SFR and sSFR respectively. From top to bottom, the blue outlined histograms in each row correspond to the M_*-, SFR-. sSFR-, and M_*-and-SFR-matched low-*z* samples (as labelled on the left axis). The upper and lower bounds of the bins used in the stacked analysis are indicated by the dashed vertical lines, whereas the mean values of the two low-*z* bins for each matched sample are indicated by the filled triangle and square, respectively. Note that the triangle represents the half with the smallest values of the global property of interest, whereas the square (with the larger number of sides) represents the bin with the larger values.

DEIMOS observations are described in more detail in Silverman et al. (2015) and Kaasinen et al. (2017), respectively.

The raw FMOS-COSMOS and COSMOS-[O II] science frames were reduced as described in Silverman et al. (2015) and Kaasinen et al. (2017), respectively. Both surveys made use of publicly available reduction pipelines to perform bias removal, flat fielding, cosmic ray rejection, and slit-tilt corrections. Wavelength calibrations were performed on a slit-by-slit basis, based on standard arc lamp

images. FMOS spectra were obtained using the publicly available FMOS image-based reduction package (`Fibre-pac`; Iwamuro et al. 2012). The DEIMOS science frames were processed via the publicly available IDL-based pipeline, `spec2d`, developed by the DEEP2 survey team (Cooper et al. 2012; Newman et al. 2013) and reduced to 1D by calculating the total flux over the effective aperture, as described in Kaasinen et al. (2017). The initial flux calibration of each (wavelength calibrated) spectrum was performed

using flux standard stars observed along with the other scientific targets (see Silverman et al. 2015; Kaasinen et al. 2017). These initial flux calibrations did not account for variable seeing conditions and atmospheric throughput.

3.2 Individual spectral analysis

Our study is based mainly on a stacked analysis of the FMOS and DEIMOS spectra (see Section 4). However, we rely on individual spectra to derive the SFRs of our sample and show the emission-line properties, metallicities and ionization parameters for the subset of galaxies with the highest S/N in the relevant emission lines in Figs 6–12. We separately derive the spectroscopic redshifts and emission-line fluxes of the two surveys. The fitting procedures for the FMOS and DEIMOS data are described in detail in Silverman et al. (2015) and Kaasinen et al. (2017), respectively. Most FMOS spectra lack stellar continuum detections and are dominated by the strongest emission lines. Because the majority of spectra lack significant detections of the stellar continuum, we used linear functions to approximate the median flux level of pixels adjacent to the emission line of interest and subtract this component prior to fitting emission lines.

We account for the effects of stellar Balmer absorption and dust extinction. To correct for $H\beta$ absorption we apply a correction factor based on the relationship derived by Zahid et al. (2014b) for the FMOS data (discussed in Section 4.2). We do not correct the $H\alpha$ flux for stellar absorption because the flux loss is negligible (<2 per cent Kashino et al. 2013). We correct for the effects of dust extinction by inferring a reddening correction from the measured Balmer decrement, $H\alpha/H\beta$, and applying the Cardelli, Clayton & Mathis (1989) extinction curve with $R_v = 3.1$. For galaxies with reliable Balmer decrements (S/N > 3 for both $H\alpha$ and $H\beta$), we estimate the level of extinction via the measured Balmer decrement and propagate the uncertainty on the Balmer decrement to the corrected line fluxes. In cases where the Balmer decrement is unreliable (either S/N($H\beta$) < 3 or $F_{\lambda_{H\alpha},0}/F_{\lambda_{H\beta},0} < 2.86$), we use upper (lower) limits on the corrected fluxes based on the upper (lower) limits of the Balmer decrements available for our sample.

3.3 Relative aperture corrections

To compare the relative fluxes from different wavelength bands, we must account for the variation in aperture size between the two surveys as well as the variation in seeing conditions on different nights. We therefore derive three separate aperture correction factors for each galaxy, corresponding to H-band ($H\alpha$ and [N II]), J-band ($H\beta$ and [O III]), and DEIMOS ([O II]) observations. All aperture correction factors are derived using the *Hubble Space Telescope* (*HST*)/Advanced Camera for Surveys (ACS) I_{F814W}-band images, smoothed according to an effective seeing. We thereby assume that the rest-frame UV and line emission have a similar spatial distribution. This assumption is partly justified by the tight correlation between the half-light radii in $H\alpha$ and the ACS I band for the SINS/zCSINF galaxies (e.g. Mancini et al. 2011). The derivation of aperture correction factors for the FMOS H- and J-band observations is described in detail in Silverman et al. (2015). We apply a similar method to derive the [O II] aperture correction factors, which we define as the ratio between the total UV flux of each galaxy and the portion of UV flux sampled by the DEIMOS slit. For each galaxy, we define a rectangular region encompassing the entire galaxy on the *HST*/ACS mosaic and take the total UV flux to be the sum of the UV flux over all pixels in this manually defined

region. To take into account the increased size of the galaxy due to the seeing conditions, we convolve each *HST*/ACS I-band image with a Gaussian point spread function (PSF) matching the seeing conditions at the time the DEIMOS observation was conducted. We determine the amount of UV flux sampled by the DEIMOS slit by summing the UV flux over the portion of the galaxy covered by the slit. The area covered by the slit is defined by the DEIMOS slit dimensions (1 arcsec× 5arcsec), the central RA and DEC, the position angle of the slit and the bounds of the galaxy itself. Based on the impact of seeing variations, the effect of the PSF used and positioning errors we apply a uniform uncertainty of ±0.05 to all aperture correction factors.

The three aperture correction factors ([O II], J band and H band) vary significantly. The mean [O II], J-band, and H-band corrections factors are 1.4, 3.7, and 2.3, respectively, for the $z \sim 1.5$ sample for which we have FMOS H- and J-band and DEIMOS observations. The difference between the aperture correction factors derived for each survey is the result of two factors: the larger physical size of the DEIMOS slit compared to the FMOS fibre and better seeing conditions for the DEIMOS observations (average of 0.75 arcsec versus 0.9arcsec). The effects of poorer seeing conditions are also apparent when comparing the two sets of aperture correction factors derived for the FMOS data. Because J-long observations were often conducted under poorer seeing conditions, most J-band correction factors for our sample are greater than the corresponding H-band correction factors.

We scale both the emission-line fluxes of individual galaxies and the spectra used for stacking by the derived aperture corrections. The relative size of the three aperture corrections means that their application may have a significant impact on the extinction corrections and individual line ratios. We ensure that the relative aperture correction factors do not bias individual emission-line flux ratios. However, we note that there is an inherent dispersion in the corrections that needs to be considered when addressing issues such as the difference in dust extinction and the width of the star-forming sequence (Fig. 1).

4 STACKING

We characterize the ISM properties of the matched low- and high-z samples based on the emission-line fluxes of stacked spectra. Of the 13 high-z galaxies for which all five lines (used to diagnose the metallicity and ionization parameter) are detected at S/N > 3, only six have sufficient S/N in the required lines after applying aperture and extinction corrections to confidently infer the ionization parameter and metallicity (see Section 5). The ISM properties of $z \sim 1.5$ star-forming galaxies are not sufficiently represented by this subset of six galaxies, which exhibit a limited range of M_* and SFR, a significant variation of inferred ISM properties and an inherent bias towards the properties of galaxies with more luminous emission lines.

By using stacked spectra, we increase the strength and S/N of the strong emission line fluxes of the sample, reduce the scatter introduced by aperture and dust corrections, and include galaxies with non-detections in some of the emission lines. The higher S/N in all five emission lines of the stacked spectra allows us to diagnose the average ionization parameter and metallicity with greater precision. By performing a stacked analysis, we assume that the single artificial galaxy spectrum created by stacking is representative of the average properties of the sample being stacked. We investigate the validity of this assumption in Section 7.1.

Table 1. Binned and stacked samples.

Sample	Sample size	Matched property	Binned property	Number per bin
High-z	50	–	M_*	25
High-z	50	–	SFR	25
High-z	50	–	sSFR	25
Low-z, M_*-matched	5000	M_*	M_*	2500
Low-z, SFR-matched	1850	SFR	SFR	925
Low-z, sSFR-matched	5000	sSFR	sSFR	2500
Low-z, M_*-and-SFR-matched	500	M_* and SFR	sSFR	250

4.1 Binning

To create the stacked spectra, we categorize the galaxies in each sample according to the global property of interest (M_*, SFR, or sSFR). For each global property, we separate the galaxies in our high-z sample into two equally sized bins, representing the halves with the low and high values of this global property. We use two bins for each high-z sample because a greater number of bins led to a significant scatter in the emission-line properties of different bins due to larger errors associated with smaller sample sizes. The final results are stable with slight changes in binning when we consider two bins for each sample.

Each matched, low-z sample is also equally separated into two bins according to the property in which it was matched to the high-z sample. The samples and bins are given in Table 1. Note that the M_*-and-SFR-matched low-z sample is separated into two bins of sSFR to allow for a 2D visual comparison with the high-z sample. We indicate the mean and the range of the matched global property spanned by each bin in Fig. 2.

4.2 Stacking high-*z* bins

We create three stacked spectra for each bin of the $z \sim 1.5$ galaxies, one each for the *H*-band, *J*-band, and DEIMOS spectra. Our method is similar to that of previous FMOS studies that rely on a stacked analysis (see Zahid et al. 2014b; Kashino et al. 2017). As noted in both these FMOS studies, a significant fraction of pixels in each FMOS spectrum are impacted by strong residual sky lines. These pixels are indentified from the noise spectra and masked out before stacking. Individual spectra are then converted to the rest frame, based on their spectroscopic redshifts, and are resampled on to a common wavelength grid. We choose wavelength spacings corresponding to the observed frame spectral resolution of FMOS (1.25 Å pixel^{-1}) and DEIMOS (0.65 Å pixel^{-1}), for galaxies at $z \sim$ 1.5. Thus, the wavelength spacings for the FMOS and DEIMOS spectra are 0.5 and 0.26 Å pixel^{-1}, respectively.

We do not fit the underlying stellar continuum or absorption, because of the lack of continuum detections in the high-z spectra. Instead, we subtract a single value for the stellar continuum for each spectrum based on the median flux in each band. The de-redshifted, resampled and continuum-subtracted spectra are scaled by their corresponding aperture correction factors (see Section 3.3). To create the final, stacked spectrum for each bin we determine the mean spectrum using idl's `resistant_mean.pro`, available from the Astronomy User's Library. Values that deviate from the median value at each pixel by more than five times the absolute deviation are removed via a 5σ clipping scheme.

The relative calibrations used while stacking are likely to be a large source of error. However, the application of aperture cor-

rections factors after continuum subtraction mean that we also rely heavily on the accuracy of the flux calibration of each band. We note that the absolute flux calibration, especially of the *J*-band spectra, may be a large source of error in the stacked spectra, leading to the selection of fewer bins of spectra to stack.

We do not correct the individual high-z spectra for Balmer absorption because of the lack of Hβ detections. However, Zahid et al. (2014b) show that the Balmer absorption of FMOS spectra becomes non-negligible for high-M_* ($M_* > 10^{10.5}$ M$_\odot$) galaxies. We therefore scale the emission-line fluxes of the stacked spectra by the absorption correction factors, $f_{\rm corr}$, predicted for the FMOS sample,

$$f_{\rm corr} = \max\{1, 1.09 + 0.30[\log(M_*/{\rm M}_\odot) - 10]\}. \quad (1)$$

based on M_* of the stacked sample. We apply the mean correction factor for the stellar masses in each bin and account for the variation in correction factors by including the standard deviation of the correction factors when deriving the uncertainty of the Hβ flux. We note that our conclusions are unaffected by the Balmer absorption corrections applied to the high-z sample.

4.3 Stacking low-*z* bins

To create the stacked low-z spectra, we use the reduced and continuum subtracted 1D SDSS spectra from the SDSS DR7 catalogue (see Stoughton et al. 2002 for details). In contrast to the high-z sample, all five emission lines of the low-z spectra are captured within a single spectrum. Thus, we do need to account for any relative aperture covering fractions for different bands. We assume that our $z > 0.04$ redshift cut-off ensures that the stacked spectra are not biased to only the central portions and create a single stacked spectrum per low-z bin. We investigate this assumption further in Section 7.1.

We do not mask out any pixels in the SDSS spectra because the emission lines are unaffected by residual skylines. Each SDSS spectrum is converted to the rest-frame wavelength based on the spectroscopic redshift. Although the SDSS spectra have been continuum subtracted using a combination of stellar population synthesis models, most of the individual spectra in our sample contain significant residual Balmer absorption features. The stellar Hβ absorption of SDSS spectra is severely underestimated, especially for galaxies with low sSFR (see discussion in Groves, Brinchmann & Walcher 2012). To remove the residual effects of the stellar absorption we fit a Gaussian profile to the underlying absorption and add the profile to the spectrum as shown in Fig. 3. Each spectrum is then resampled to a common wavelength grid of 1.5 Å (as in Geller et al. 2014). Like the stacked high-z spectra, our stacked low-z spectra are created by taking the mean of the resampled and de-redshifted spectra for each bin via the 'resistant_mean' algorithm with a 5σ clipping scheme.

We show the extent of our corrections to the residual Balmer absorption for the low-z matched samples in Fig. 4, via the absorption correction factor ($F({\rm H}\beta_{\rm corr})/F({\rm H}\beta)$). The mean absorption correction factors of the low-z SDSS galaxies increase with M_* but scale inversely with sSFR. However, we note that there is a significant spread in the absorption correction factors of high mass ($M_* > 10^{10.5}$ M$_\odot$) low-z galaxies. This spread is the result of the spread in sSFRs. High-mass galaxies in only the sSFR-matched sample require significantly less correction for Balmer absorption than the majority of high-mass low-z galaxies, which have lower sSFRs. In fact, the mean correction factors of the low-z, sSFR-matched sample are consistent with the relation derived for the
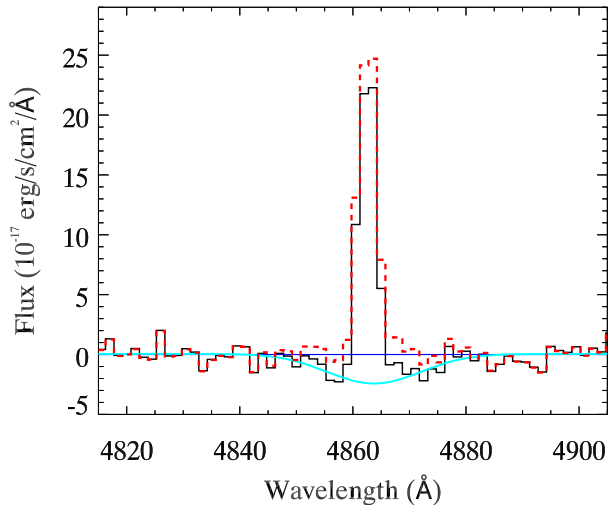
Figure 3. Example of the effect of Balmer absorption on a single low-z galaxy spectrum. The fit to the Balmer absorption (solid cyan line) is added to the measured spectrum (solid black line) resulting in a spectrum with a larger Hβ emission feature (red dashed line).

FMOS sample (dashed red line), which exhibits the same range of sSFRs. The offset of the absorption correction factors of the entire matched low-z sample (filled circles) from the FMOS relation therefore reflects the lower sSFRs of most galaxies in the matched, low-z samples.

4.4 Emission-line fluxes of stacked bins

We fit the emission lines of the low- and high-z stacked spectra in three separate wavelength regimes, around; (1) [O II], (2) Hβ and [O III]λ5007, and (3) Hα and [N II]λ6584. We use IDL's mpcurve-fit.pro to fit the supplied Gaussian functions. To extract the emission-line fluxes of the [O II] doublet, we assume a double Gaussian profile. For the Hβ and [O III]$\lambda\lambda$4959, 5007 fits, we apply a single Gaussian profile to each line and fix the relative amplitudes of the [O III] lines to the laboratory value of 2.887 (Tachiev & Fischer 2001). Similarly, we fit Hα, [N II]λ6548, [N II]λ6584 with single Gaussian functions and fix the relative amplitude of the [N II] lines to the laboratory value of 2.941 (Tachiev & Fischer 2001; Kramida et al. 2015). We use a single full width at half-maximum (FWHM) to describe the widths of the lines in each wavelength regime but note that the values of FWHM may differ for the three wavelength regimes. We ensure that the emission-line fluxes of stacked spectra were consistent with the sum of the emission-line fluxes derived for individual FMOS spectra for subsamples consisting of spectra with all emission lines detected at S/N > 3. The stacked spectra and corresponding emission-line fits of the lowest mass bin of low- and high-z stacked spectra are shown in Fig. 5.

We estimate the errors on the emission-line fluxes of stacked spectra via a bootstrapping technique. For each stacked spectrum, we generate 1000 additional stacked spectra, each constructed from a random sample of galaxies drawn with replacement from the sample used for the actual stacked spectrum. We take the errors on the aperture corrections into account when constructing the additional spectra. To avoid biasing the results for the smaller bin sizes of the high-z sample, we ensure that no more than six of the 25 galaxies in each bin are replaced with duplicates. For each additional spectrum, we re-fit the emission lines as for the real spectrum. The errors on the measured emission-line fluxes are taken to be the standard deviation

of the distribution of emission-line fluxes for the additional spectra. Our choice of the number of additional spectra and percentage to resample ensures that our errors are approximately Gaussian.

We correct the emission-line fluxes of the stacked spectra for extinction based on the Balmer decrement of each stacked bin of galaxy spectra. We assume an intrinsic Balmer decrement of Hα/Hβ = 2.86, consistent with Case B recombination at $T = 10^4$ K and n_e = 100 cm^{-3} (Dopita & Sutherland 2003; Osterbrock & Ferland 2006), and apply the Cardelli et al. (1989) extinction curve with R_v = 3.1. The results of this study are not dependent on our choice of a particular extinction law but are highly sensitive to the value of the Balmer decrement for each stacked bin. We ensure that the mean Balmer decrement of the individual low-z spectra that make up each bin are consistent with the Balmer decrement derived for their stacked spectra. We therefore assume that the extinction corrections applied to the stacked spectra are representative of the sample and not biased towards a subset of galaxies. Because of the limited number of Hβ detections in the high-z sample we are unable to make the same comparison between the average and stacked Balmer decrements. However, we note that the variation in Balmer decrements between different bins of high-z galaxies follows the correlation with SFR. The Balmer decrements of the stacked high-z bins vary from ~3.8 to 5.1, with higher values corresponding to bins containing galaxies with higher SFRs or stellar masses. The minimum value is consistent with the mean Balmer decrement of the subset of the high-z sample for which we measure both Hβ and Hα at S/N $\geq$ 3, $F_{\text{H}\alpha}/F_{\text{H}\beta} \sim$ 3.8. We conclude that the Balmer decrements of the stacked high-z bins are reasonable and take into account the larger uncertainties, compared to the stacked bins of low-z galaxies, when performing extinction corrections.

To estimate the errors on the extinction corrected emission-line fluxes we use a Monte Carlo resampling technique. We perturb all five measured emission-line fluxes with the errors estimated from bootstrapping, and use the new Balmer decrement to correct the perturbed line fluxes. We repeat this process 1000 times to build a well-sampled distribution of corrected emission-line fluxes and take the standard deviation of the these corrected fluxes to be the errors on the emission-line fluxes for each bin.

4.5 AGN contamination

We did not apply the [O III]/Hβ and [N II]/Hα ratios to investigate the AGN contamination for the majority of the high-z sample, which lacked detections of either Hβ, [O III], or [N II]. We therefore investigate the extent of any remaining AGN contamination by comparing the position of our stacked samples to the theoretical maximum position of $z \sim 1.5$ star-forming galaxies on the BPT diagram from (Kewley et al. 2013b) (dashed black line, Fig. 6). Regardless of the property in which the samples are binned, the stacked data lie below the theoretical maximum position predicted at $z \sim 1.5$ predicted by Kewley et al. (2013b). Moreover, the stacked samples are offset to lower [O III]/Hβ than the $z \sim 2.3$ sample of Steidel et al. (2014) (orange line in Fig. 6).

5 DERIVING METALLICITIES AND IONIZATION PARAMETERS

To investigate the evolution of the ionization parameter, we apply diagnostic methods that simultaneously constrain both the ionization parameter and metallicity. We infer the metallicity in order to take into account its effect on the ionization parameter and to account for the degeneracies between emission-line ratios and the metallicity
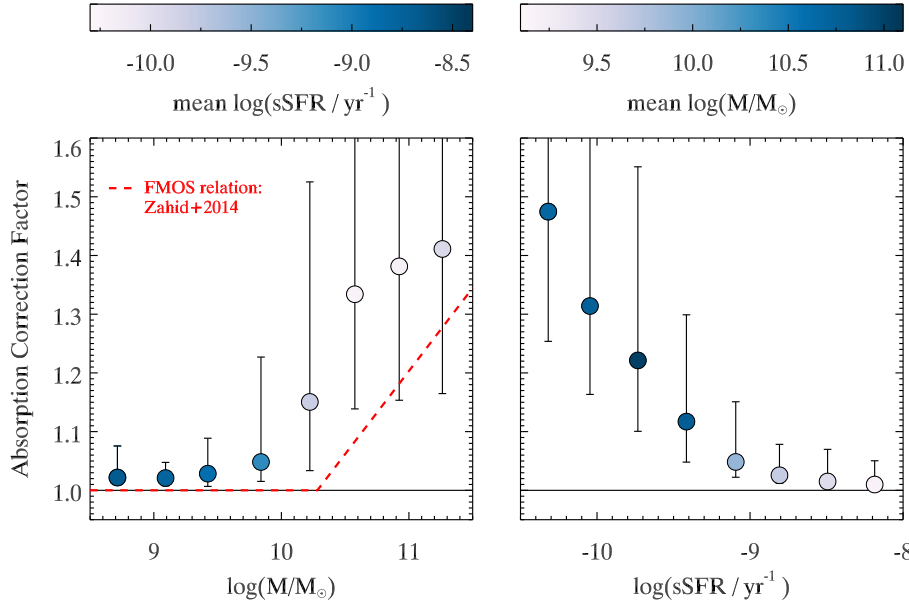
Figure 4. Balmer absorption correction factor [$F(H\beta_{corr})/F(H\beta)$] per bin of M_* (left-hand panel) and sSFR (right-hand panel) for galaxies in the four low-z matched samples. Filled circles indicate the mean absorption correction factor per bin, with error bars extending to the 16th and 84th percentile values. The mean sSFR of the M_* bins in the left-hand panel is indicated by the shading described in the top left colour bar, whereas the mean M_* of the sSFR bins in the right-hand panel is indicated by the shading described in the top right colour bar. The corrections factors derived for the low-z matched samples are compared to the relationship derived for the $z\sim 1.5$ FMOS sample of Zahid et al. (2014a; equation 1, dashed red line).
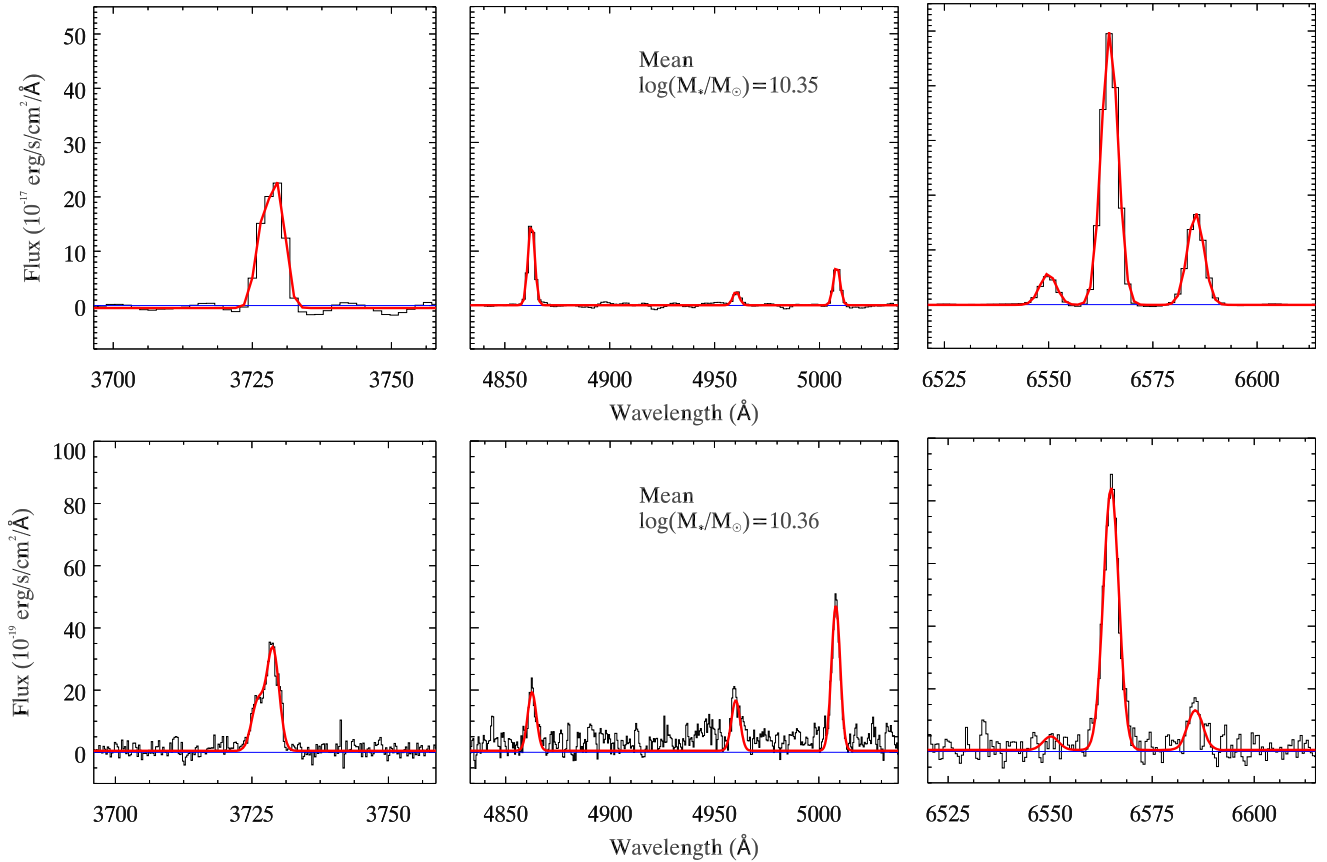
Figure 5. Stacked spectra (solid black) of the lowest mass bin of the low-z M_*-matched (top row) and high-z (bottom row) samples compared to the emission-line fits (solid red). The three panels in each row indicate the three fitting windows used to fit the five emission lines. Left-hand panel: [O II]$\lambda\lambda$3726, 3729 fit. Middle panel: Hβ and [O III]$\lambda\lambda$4959, 5007. Right-hand panel: [N II]$\lambda\lambda$6548, 6584 and Hα.
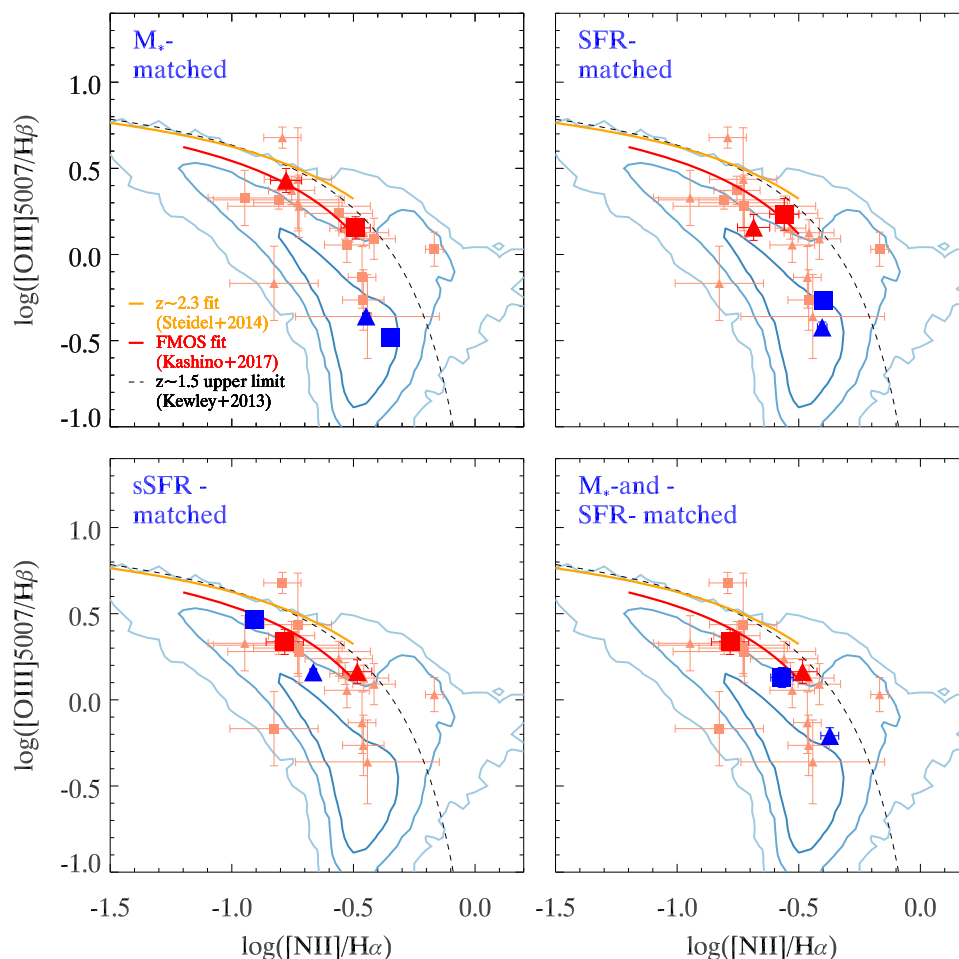
Figure 6. [O III]λ5007/Hβ versus [N II]λ6584/Hα for the stacked matched local (blue) and z∼ 1.5 (red) samples. Each panel shows the ratios derived from stacks of spectra binned in different quantities and matched as labelled at the top left. The emission-line ratios of the stacked spectra (large filled symbols) are compared to the individual measurements of the high-z galaxies with Hβ, [O III]λ5007, Hα, and [N II]λ6584 detected at S/N ≥ 3 (small, light red filled symbols) and the distribution of the 'low-z star-forming catalogue' (1,2 and 3σ limits represented by the light to dark blue contours). The symbols of the individual high-z galaxies indicate which bin they are assigned to, where triangles(squares) indicate galaxies assigned to the low (high) M_*, SFR or sSFR bins. The fits to z ∼ 2.3 data from Steidel et al. (2014; solid orange), the z ∼ 1.5 FMOS sample of Kashino et al. (2017) and the maximum theoretical ratios from Kewley et al. (2013; solid black) are shown for comparison. Upper left: binned in M_*. Upper right: binned in SFR. Lower left: binned in sSFR. Lower right: M_*-and-SFR-matched, binned in sSFR.

and ionization parameter. Although there exist numerous diagnostic methods which allow the metallicity to be inferred from the relative strengths of strong emission lines (see Kewley & Ellison 2008 and Dopita et al. 2013 for discussions on metallicity diagnostics), the range of ionization parameter diagnostics is far more limited. There currently exist three options for inferring the ionization parameter, based on theoretical models of H II regions. The first two options are the theoretically calibrated diagnostics of Kewley & Dopita (2002) and Kobulnicky & Kewley (2004). The third option is to use an algorithm that compares a user-supplied model grid of emission-line fluxes and ISM properties to the measured fluxes, e.g. IZI (Blanc et al. 2015) and pyqz (Vogt et al. 2014).

We apply two diagnostic methods to infer ionization parameters and metallicities. Both diagnostic methods rely on theoretical photoionization models of idealized H II regions are sensitive to variations in metallicity and ionization parameter and employ the five emission lines available for our high-z sample ([O II]λ3727, Hβ, [O III]λ5007, Hα, and [N II]λ6584). Our first method employs the IDL-based Bayesian inference algorithm, IZI,

developed by Blanc et al. (2015). Our second method makes use of the calibration of the O_{32} and R_{23} ratios from Kobulnicky & Kewley (2004), as described in Kewley & Ellison (2008). We refer to the second diagnostic as KK04 diagnostic hereafter.

5.1 IZI

We use IZI to infer the metallicity and ionization parameter of the stacked galaxy samples based on the dust corrected emission-line fluxes and our theoretical photoionization model grids. The formalism and statistical method employed by IZI are presented in detail in Blanc et al. (2015). By using IZI, we avoid some of the systematic uncertainties associated with the calibration of diagnostics based on a single strong emission line ratio (Dopita et al. 2006b, 2006a; Vogt et al. 2014; Blanc et al. 2015) and apply a model of our choice that is based on the most up-to-date atomic data and solar abundances. Moreover, most strong emission-line diagnostics are unable to account for the asymmetry of the error bars on the derived parameters. Because IZI performs a full calculation of the

joint probability distribution function (PDF) of Z and $\log(q)$, we are able to investigate the topology of the joint PDFs and account for any asymmetries.

We provide IZI with theoretical photoionization models, based on multiple simulations of H II regions using the MAPPINGS V photoionization code, version 5.1.02. Our models are a subset of the 'pressure models' described in detail in Kewley (in preparation). In brief, we use the Starburst99 (SB99) models described in Levesque, Kewley & Larson (2010) and Nicholls et al. (2013) and apply the stellar atmosphere models and tracks described in Kewley (in preparation). Our models are based on a Salpeter IMF Salpeter (1955) with an upper mass limit of $100\,M_\odot$, but the choice of IMF has negligible impact on the optical emission-line fluxes used in our analysis. To account for the depletion of metals by dust as well as the impact on the cooling rate, we assume a base depletion of $[\text{Fe/H}] = -1.5$ dex and apply the corresponding dust depletion model of Jenkins (2013). Our simulations are based on continuous star formation models because these are more representative of the multiple sites of ongoing star formation in star-forming galaxies than instantaneous bursts of star formation. We use an oxygen abundance scale and assume a bulk solar oxygen abundance of $12 + \log(\text{O/H}) = 8.73$ consistent with the primordial solar abundance of Asplund et al. (2009). Our simulations are performed using a standard Maxwellian electron energy and assume a plane parallel geometry (as for the models used in the KK04 diagnostic).

To account for the sensitivity between the ionization parameter, metallicity, and ISM pressure (see Dopita et al. 2006b; Kewley et al. 2013b), we perform simulations that encompass a range of these parameters. Our simulated H II regions have a detailed electron temperature and density structure that varies through the nebula based on the metallicity and the ionizing radiation field. The ISM pressure in our simulated H II regions (P/k) reflects the mechanical energy flux produced by the stellar population (see also Kewley, in preparation). The model metallicities are constrained by the stellar tracks used in the stellar population synthesis models. Our simulated H II regions span the following values of metallicity, ionization parameter, and pressure:

$$12 + \log(\text{O/H}) = \{7.63, 8.23, 8.53, 8.93, 9.23\},$$
$$\log\left(q\,/\,\text{cm}\,\text{s}^{-1}\right) = \{6.50; 6.75; 7.00; 7.25; 7.50;$$
$$7.75; 8.00; 8.25; 8.50\},$$
$$\log([P/k]/\,\text{cm}^{-3}\,\text{K}) = \{5.0, 5.5, 6.0, 6.5, 7.0, 7.5, 8.0\}.$$

It is beyond the scope of this work to simultaneously diagnose the ISM pressure as well as the metallicity and ionization parameter. We therefore choose the appropriate ISM model pressure based on the relationships between the ISM pressure and the [S II]λ6717/[S II]λ6731 and [O II]λ3729/[O II]λ3726 ratios given in Kewley (in preparation). The relationship between the doublet ratios and ISM pressure depends upon the metallicity and ionization parameter, as shown in figs 9 and 13 of Kewley (in preparation). These relationships can be parametrized by functions of the doublet ratio, $12 + \log(\text{O/H})$ and $\log(q)$. Based on the expected metallicity and ionization parameter regimes $8.5 < 12 + \log(\text{O/H}) < 8.9$ and $6.5 < \log(q/\text{cm}\,\text{s}^{-1}) < 8.5$ (see results from KK04 diagnostic, Figs 9–11), we predict the ISM pressures using the [S II]λ6717/[S II]λ6731 and [O II]λ3729/[O II]λ3726 ratios. The median [S II]λ6717/[S II]λ6731 ratios of the M_*-matched, SFR-matched, sSFR-matched, and M_*-and-SFR-matched samples are $\sim$1.39, 1.29, 1.35, and 1.29, respectively, corresponding to ISM pressures of $P/k \sim 10^6$, $10^{6.5}$, $10^{6.5}$, and $10\,\text{cm}^{-3}\text{K}$ (see Kewley $^{6.5}$in preparation). The median (and mean) [O II]λ3729/[O II]λ3726 ratio

of the high-z sample is $\sim$1.2 corresponding to an ISM pressure of $\sim$10^{6.5}\,\text{cm}^{-3}\,\text{K}$.

We perform various tests before applying IZI to our stacked samples. First, we ensure that when using the model fluxes as an input to IZI the inferred values of Z and $\log(q)$ are those of the models. Secondly, we test the effect of increasing the errors and perturbing the input line fluxes by the errors. In order for the metallicity and ionization parameter to be well constrained (<0.3 dex), we require [O II]λ3727, Hβ, [O III]λ5007, Hα, and [N II]λ6584 to be measured at S/N ≥ 5. We also test the effects of using different combinations of strong emission-line fluxes. The choice of input line fluxes has a significant impact upon the derived values of Z and $\log(q)$. The use of the [S II]$\lambda\lambda$6717, 6731 flux, in addition to the other five lines, results in more accurate inferences of the metallicity (judged against the simulated H II regions), especially in cases where the metallicity lies near the peak of the R_{23} versus $12 + \log(\text{O/H})$ curve. The difference in inferred metallicities was up to 0.2 dex. However, the addition of [S II] had no noticeable impact on the ionization parameter. The omission of [N II] led to significant differences in metallicity (by up to 0.6 dex for individual galaxies) but had less effect on the ionization parameter (up to 0.3 dex). In contrast, the omission of [O III] or [O II] greatly changed the measured ionization parameter by $\delta\log(q) \sim 0.5$ dex.

To allow for an unbiased comparison between the low- and high-z stacked samples, we employ only the five emission lines measured for the $z \sim 1.5$ sample. We supply IZI with the dust-corrected emission-line fluxes and errors as well as the most suitable photoionization model (based on the electron density). The error on our model emission-line fluxes is 0.05 dex. We confirm that the inferred values of Z and $\log(q)$ for each stacked sample are single-valued, bounded and represent a clear maximum in the joint 2D PDF. The uncertainties on Z and $\log(q)$ represent the separation between the joint mode of Z and $\log(q)$ and the 1σ confidence interval (described in Blanc et al. 2015). In cases where the errors on Z are more extended (>0.3 dex), the metallicity lies close to the peak of the R_{23} versus $12 + \log(\text{O/H})$ curve.

5.2 KK04 diagnostic

We also infer ionization parameters and metallicities using the KK04 diagnostic (Kobulnicky & Kewley 2004). The KK04 diagnostic method is based on two line ratios: the ionization parameter sensitive $O_{32} = $ [O III]$\lambda\lambda$4959, 5007/[O II]$\lambda\lambda$3726, 3729 ratio and metallicity sensitive $R_{23} = $ [O III]$\lambda\lambda$4959, 5007 + [O II]$\lambda\lambda$3726, 3729/Hβ ratio. To derive the relationship between these line ratios and the values of Z and $\log(q)$, Kobulnicky & Kewley (2004) applied the photoionization grids of Kewley & Dopita (2002). These photoionization models assume a single-ISM pressure of $P/k = 10^5\,\text{cm}^{-3}\,\text{K}$. The models are described in detail in Kewley & Dopita (2002).

Because the R_{23} and O_{32} ratios are sensitive to both the metallicity and ionization parameter, the iteration over both calibrations allows the metallicity and ionization parameter to be jointly constrained. However, the R_{23} ratio is double valued with metallicity (see Kewley & Dopita 2002; Dopita et al. 2006a,b) and thus the KK04 method requires an initial metallicity guess to determine the branch over which to iterate. To determine the initial branch we use both the [N II]/Ha and [N II]/[O II] ratios as described in the appendix of Kewley & Ellison (2008). For each binned and stacked set of emission-line fluxes, the two [N II]-based line ratios result in the same initial guess of metallicity branch, namely the upper

branch ($12 + \log{(O/H)} > 8.5$, Kewley & Dopita 2002; Kobulnicky & Kewley 2004).

The uncertainty on the values of Z and $\log{(q)}$ inferred from the KK04 diagnostic tend to be smaller than the 1σ confidence intervals which result when using IZI. The comparitively smaller uncertainties are the result of a combination of factors. First, the metallicity branch is chosen before the KK04 diagnostic iterations are applied, and thus, there is no uncertainty in the choice of the branch. Secondly, the uncertainties derived for the KK04 diagnostic are based solely on the errors on the emission-line fluxes and do not reflect the uncertainty of the models or the how well the data matches the models.

6 RESULTS

6.1 Emission-line ratios

We compare the emission-line ratios of the matched low- and high-z stacked samples in Figs 6–8. We focus on three emission-line ratio diagrams; the [O III]/Hβ versus [N II]/Hα, or 'BPT' diagram (Baldwin, Phillips & Terlevich 1981), the O_{32} versus R_{23} diagnostic diagram and the [N II]/[O II] versus [O III]/Hβ diagram. The BPT diagram is commonly used to assess the dominant ionization source of a galaxy, such as the presence of AGN. However, the position of galaxies on the BPT diagram is also sensitive to the metallicity, ionization parameter, and pressure (discussed in detail in Kewley et al. 2013b). The O_{32} versus R_{23} diagnostic diagram is commonly used to trace the ionization parameter and metallicity, because the O_{32} ratio is highly sensitive to the ionization parameter whereas the R_{23} is highly sensitive to metallicity (Kewley & Dopita 2002; Nakajima & Ouchi 2014; Shapley et al. 2015; Sanders et al. 2016). However, the O_{32} versus R_{23} diagram is not a clean diagnostic because the O_{32} ratio is dependent on metallicity and the R_{23} diagnostic is dependent on the ionization parameter (Kewley & Dopita 2002; Kewley, in preparation). The [N II]/[O II] versus [O III]/Hβ diagnostic diagram is mostly sensitive to the metallicity and ionizing radiation source (see Dopita et al. 2013) but may also be a useful comparison of different galaxy samples (e.g. Shapley et al. 2015). Shapley et al. (2015) argue that the an offset in [N II]/[O II] may indicate a difference in the N/O ratio at fixed metallicity. We do not interpret the [N II]/[O II] versus [O III]/Hβ diagram in the same manner. Instead, our work is based on the abundance scaling of N/O versus O/H discussed in Nicholls et al. (2017).

The consistency between the positions of matched low- and high-z samples on the [O III]/Hβ and [N II]/Hα diagram varies according to the property in which the samples are matched (red versus blue symbols in Fig. 6). For samples matched in M_*, the high-z bins exhibit $\sim$0.7 dex larger [O III]/Hβ ratios and $0.2-0.3$ dex smaller [N II]/Hα ratios than the equivalent low-z bins of M_* (top left-hnad panel). Similarly, for samples matched in SFR, the high-z bins exhibit $\sim$0.5 dex higher [O III]/Hβ and $0.1-0.3$ dex lower [N II]/Hα ratios than the corresponding low-z bins (top right-hand panel). In contrast, samples matched in sSFR exhibit consistent [O III]/Hβ ratios and show the opposite trend for [N II]/Hα (bottom left-hand panel). The [N II]/Hα ratios of the high-z sSFR bins are $\sim$0.1 dex higher than for the equivalent sSFR bin of low-z galaxies. For samples matched in both M_* and SFR, the high-z bins exhibit $\sim$0.2 dex larger [O III]/Hβ and 0.2 dex smaller [N II]/Hα ratios than the matched low-z bins (bottom right-hand panel).

The property in which the low- and high-z samples are matched also affects their relative positions on the O_{32} versus R_{23} diagram (Fig. 7). Both M_* bins of the high-z samples exhibit significantly

higher O_{32} ratios, $0.7-0.8$ dex and $0.2-0.3$ dex higher R_{23} ratios than the equivalent M_* bins of low-z galaxies (top left-hand panel). For samples matched in SFR, the high-z bins exhibit $\sim$0.6 dex larger O_{32} and 0.2 dex larger R_{23} ratios than the equivalent low-z bins (top left-hand panel). In contrast, the positions occupied by the low- and high-z samples matched in sSFR are very similar, with the high-z bins of sSFR exhibit equivalent O_{32} (within errors) and <0.1 dex lower R_{23} ratios than the low-z bins.

As for the other emission-line ratio diagrams, we find that the positions occupied by the low- and high-z matched samples on the [N II]/[O II] versus [O III]/Hβ diagram are more closely matched for samples with equivalent sSFR (Fig. 8). For the M_*-matched samples, there is a greater offset between the [O III]/Hβ ratios of the low- and high-z sample than the [N II]/[O II] ratios ($\sim$0.6 dex versus $0.2-0.4$ dex). Similarly, for samples matched in SFR, the [O III]/Hβ ratios of the high-z sample are greater by $\sim$0.5 dex, whereas the [N II]/[O II] ratios are smaller by $\sim$0.3 dex. In contrast, the positions occupied by each bin of the sSFR-matched and M_*-and-SFR-matched low-z samples are consistent with the corresponding high-z bins, varying by $\leq$0.3 dex in either ratio (bottom row). The sSFR-matched and M_*-and-SFR-matched samples exhibit slight offsets in opposite ratios. The [N II]/[O II] ratios of the low- and high-z samples with equivalent sSFR is slightly offset, whereas the offset between the M_*-and-SFR-matched samples is only in [O III]/Hβ. In addition, the positions occupied by low-z sSFR-matched sample are consistent with individual galaxies in the high-z sample.

The differences in the [O III]/Hβ, O_{32}, and R_{23} ratios of the M_*-matched low- and high-z samples suggests that there is a significant evolution in the ionization state of main-sequence galaxies from $z \sim 0.1$ to $z\sim 1.5$. However, once the sSFR is taken into account, the low- and high-z samples exhibit equivalent [O III]/Hβ and O_{32}. This suggests the evolution in sSFR is one of the main factors driving the observed offset of emission-line ratios at high redshift.

6.2 Comparison with previous work

The differences between our low-z stacked samples, and between the two bins within each sample, are consistent with previous studies of the position of galaxies on the BPT and O_{32} versus R_{23} diagrams. Dickey et al. (2016), Liu et al. (2008), and Brinchmann et al. (2008) show that the position of galaxies on these diagrams is strongly correlated with the level of star formation activity, assessed via the sSFR, SFR surface density (Σ_{SFR}), or excess EW(Hα). Galaxies with higher levels of star-formation activity relative to typical star-forming galaxies of the same stellar mass (and at the same epoch) tend to lie above the local star-forming abundance sequence on the BPT diagram (Brinchmann et al. 2008; Liu et al. 2008), exhibiting both higher [O III]/Hβ (Dickey et al. 2016) and O_{32} ratios (Nakajima & Ouchi 2014; Sanders et al. 2016) than the more typical low-z, star-forming galaxies. Likewise, we find that the low-z, sSFR-matched sample exhibits significantly higher [O III]/Hβ, O_{32}, and R_{23} ratios than either bin of the M_*-matched sample, which has a lower mean sSFR (blue filled symbols in top versus bottom left-hand panels of Figs 6 and 7). Moreover, the high sSFR bin of the sSFR-matched sample exhibits higher [O III]/Hβ O_{32} and R_{23} than the low sSFR bin (triangle versus square in bottom left-hand panel of Figs 6 and 7).

The position of our high-z sample on the diagnostic diagrams is also consistent with previous theoretical and high-z observational studies (e.g. Kewley et al. 2013b; Masters et al. 2014; Dickey et al. 2016; Sanders et al. 2016; Kashino et al. 2017). Our high-z sample (both individual and stacked) exhibits higher [O III]/Hβ ratios, higher O_{32} and lower [N II]/Hα than the majority of low-
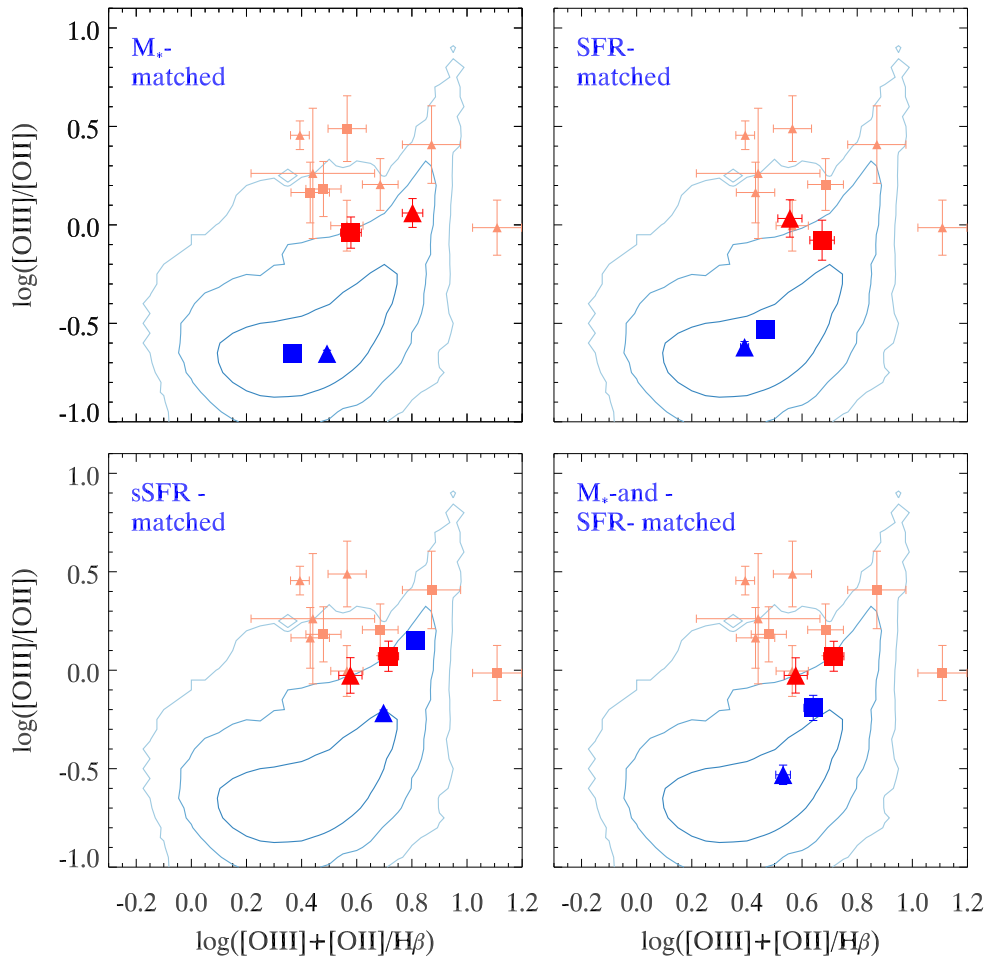
Figure 7. $O_{32} = \log([\text{O III}]\lambda\lambda4959, 5007/[\text{O II}]\lambda\lambda3726, 3729)$ versus $R_{23} = \log([\text{O III}]\lambda\lambda4959, 5007 + [\text{O II}]\lambda\lambda3726, 3729/\text{H}\beta)$ for the four matched local (blue) and $z \sim 1.5$ (red) samples. Each panel shows different binned and stacked samples as labelled at the top left. The emission-line ratios of the stacked spectra (large filled symbols) are compared to the individual measurements of the high-z galaxies with [O II], H β and [O III]$\lambda5007$ detected at S/N $\geq$ 3 (small, light red filled symbols). The four panels, blue contours, and symbols are the same as in Fig. 6.

z, star-forming galaxies (blue contours in Figs 6 and 7), and the M_*-matched sample. Assuming that the star-forming abundance sequence (on the BPT diagram) increases with redshift, as suggested by Kewley et al. (2013a), then we would also expect our sample to lie between the local sequence and the $z \sim 2.3$ sample of Steidel et al. (2014). We find that our sample of high-z galaxies indeed lies below the $z \sim 2.3$ sample of Steidel et al. (2014) (see the orange line in Fig. 6). Moreover, our high-z sample occupies comparable positions on the O_{32} versus R_{23} and [N II]/[O II] versus [O III]/H β diagrams to the $z \sim 2.3$ MOSDEF sample presented in Shapley et al. (2015) and Sanders et al. (2016), although our individual detections exhibit greater scatter and lower S/N.

6.3 Metallicities

We compare the metallicity of each matched bin of low- and high-z galaxies in the top rows of Figs 9–12. Each matched low- and high-z bin is represented by the same symbol, with the low-z sample in blue and the high-z bin in red. For comparison, we show the average metallicity of the M_*-, SFR-, sSFR-, and M_*-and-SFR-matched, low-z samples as a function of the matched property (blue solid and dashed lines). The individual metallicities of each low-z

matched sample are derived via the same methods as for the stacked bins. We also show the subsample of high-z galaxies for which we can individually diagnose the metallicity and ionization parameter.

The offset between the metallicities of the low- and high-z samples varies according to the property in which they are matched. The M_*-matched, low-z bins exhibit $0.15-0.3$ dex higher metallicities than the matched high-z bins and the SFR-matched, low-z bins exhibit 0.15 dex higher metallicities than the equivalent high-z bins. In contrast, the sSFR-matched low-z bins exhibit $0.1-0.2$ dex lower metalliciThe ensueing studies havetyes than the corresponding high-z bins. For the M_*-and-SFR-matched samples, the low- and high-z bins have metallicities that are consistent within the errors.

The metallicity of the M_*-matched samples increases with M_*, consistent with previous studies of the MZ relation (e.g. Tremonti et al. 2004; Zahid et al. 2013; Zahid et al. 2014b; Kashino et al. 2017). For both the low- and high-z stacked samples, the higher stellar mass bin exhibits a higher metallicity than the low-mass bin. Likewise, the average metallicity of the M_*-matched sample and full low-z star-forming catalogue increases as a function of metallicity, consistent with the MZ relation of Zahid et al. (2013). We also find a significant offset between the metallicity of the low- and high-z matched samples, consistent with the evolution of the MZ relation observed by Zahid et al. (2013).
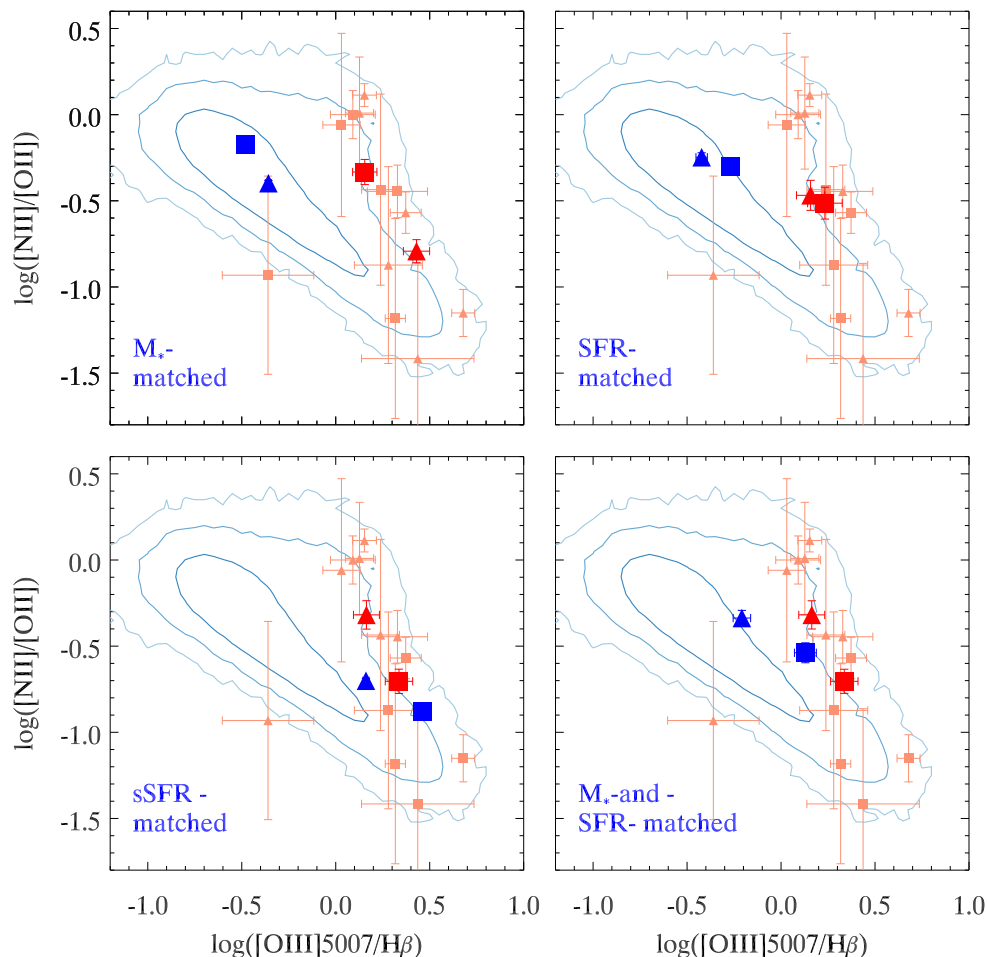
Figure 8. [N II]λ6584/[O II]λ3727 versus [O III]λ5007/H β for the four matched local (blue) and z∼ 1.5 (red) samples. Each panel shows different binned and stacked samples as labelled at the top left. The emission-line ratios of the stacked spectra (large filled symbols) are compared to the individual measurements of the high-z galaxies with [O II], H β and [O III]λ5007 and [N II]λ6584 detected at S/N ≥ 3 (small, light red filled symbols). The four panels, blue contours, and symbols are the same as in Fig. 6.

The difference between the metallicities of the matched low- and high-z bins is independent of the diagnostic method used. However, the exact values of metallicity are offset between the diagnostics, with the KK04 diagnostic predicting ∼0.1 dex higher metallicities than IZI for each stacked bin. There are three main reasons for the discrepancy between the diagnostics: the models on which the diagnostics are based, the use of the measured emission lines, and the choice of grid pressure.

We test the effects of the difference between the models via the two diagnostics using a sample of H II regions from van Zee et al. (1998). To evaluate the difference between the models we restrict IZI to the [O II], H β, and [O III] lines, used by the KK04 diagnostic. We apply the log $P/k = 5$ pressure grid, the same ISM pressure used for the KK04 diagnostic, and use only the 136 (out of 188) H II regions which lie on the upper metallicity branch $12 + \log (O/H) > 8.3$. To ensure that IZI chooses the correct branch we apply a step function prior on the metallicity (see also Blanc et al. 2015). Based on the same set of lines, the KK04 diagnostic predicts 0.13 dex higher metallicities, on average, than IZI, with a dispersion of 0.03 dex about the mean offset. The difference between the two diagnostics when using the same lines is due to the stellar evolution and photoionization model revisions that have occurred between 2002 and 2017, which include the introduction of metal opacities in the stellar

atmospheres, updated atomic data and abundance sets in the photoionization models, and a more detailed treatment of dust physics during radiative transfer calculations.

The second difference between the diagnostics applied to the stacked samples is the treatment of the [N II] and H α lines. The KK04 diagnostic gives all the weight to the relative strengths of [O II], H β, and [O III] via the O_{32} and R_{23} ratios, whereas we also account for the effect of [N II]/[O II] and [N II]/H α when using IZI. Both the [N II]/[O II] and [N II]/H α ratios are highly sensitive to the metallicity and therefore allow for more accurate inferences of the metallicity (e.g. Dopita et al. 2013; Blanc et al. 2015). The addition of the [N II] flux as an input to IZI when diagnosing the metallicities of the 136 H II regions (on the upper metallicity branch) from van Zee et al. (1998) resulted in an increased metallicity offset, of 0.24 dex, with a dispersion of 0.13 dex. We note that the additional use of the [S II] flux resulted in a similar metallicity offset of 0.23 dex, with a dispersion of 0.13 dex about the mean offset.

6.4 Ionization parameters

We compare the ionization parameters of each matched bin of low- and high-z galaxies in the bottom rows of Figs 9–12. Each matched low- and high-z bin is represented by the same symbol, with the
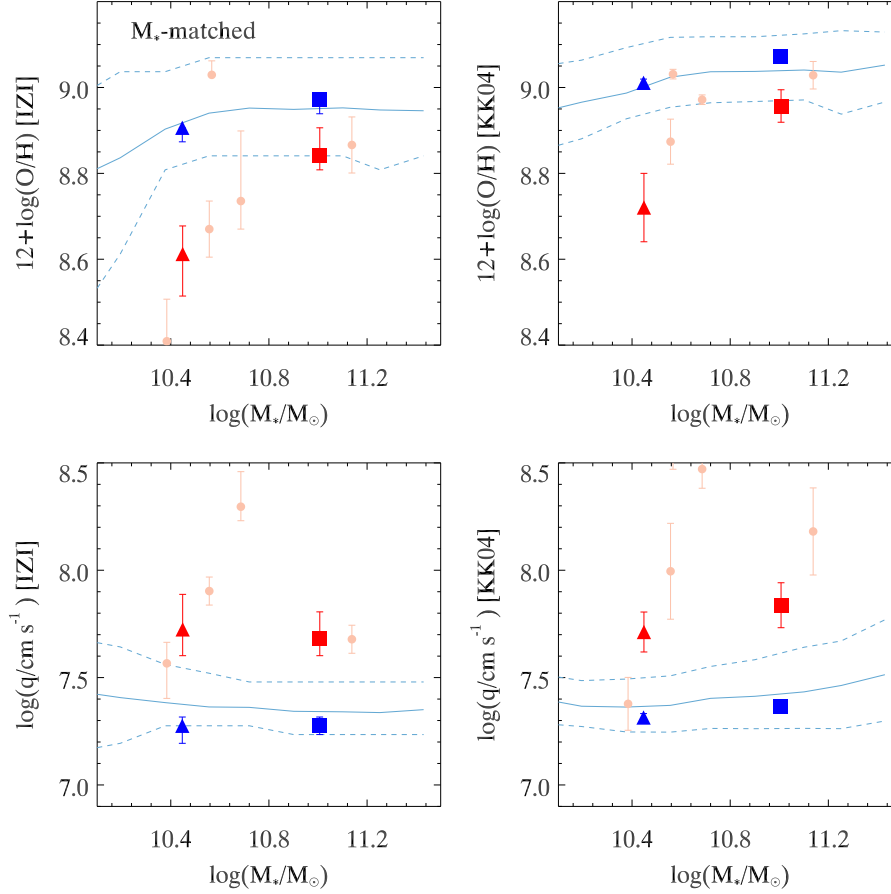
Figure 9. Metallicity and ionization parameter as a function of M_* for the M_*-matched low-z (blue filled symbols) and high-z (red filled symbols) samples. The subset of $z\,1.5$ galaxies for which q and Z could be inferred individually is shown for comparison (pink filled symbols). Left column: results from the IZI diagnostic. Right column: results based on the KK04 diagnostic. The symbols for the three bins are consistent with those in the top row of Fig. 2. The mean metallicity and ionization parameter (solid, light blue line), 16th and 84th percentiles (dashed light blue line) of the M_*-matched, SDSS sample derived via IZI (left-hand panels) and the KK04 diagnostic (right-hand panels) are shown as a function of M_* for comparison.

low-z sample in blue and the high-z bin in red. For comparison, we show the average ionization parameter of the M_*-, SFR-, sSFR-, and M_*-and-SFR-matched, low-z samples as a function of M_*, SFR, sSFR, and sSFR, respectively (blue solid and dashed lines) derived via the same methods as for the stacked bins. We also show the subsample of high-z galaxies with high enough S/N in all five lines to individually diagnose the metallicity and ionization parameter.

The ionization parameters of the low- and high-z samples are only consistent for samples matched in sSFR. We recover an offset of 0.3–0.5 dex in the ionization parameter between the high-z sample and M_*-matched low-z sample (Fig. 9). Thus, we show that there is an evolution of $\sim$0.4 dex in the ionization parameter of main-sequence galaxies from $z \sim 0.1$ to $z\sim 1.5$. We recover a similar offset, between the high-z sample and SFR-matched low-z sample, although the highest SFR bin of the SFR-matched samples is more closely matched than the lowest SFR bin. The ionization parameters of low- and high-z bins matched in both M_* and SFR are more closely matched than for either the M_*- or SFR-matched samples (bottom row, Fig. 12). We note that the sSFRs of the low-z M_*-and-SFR-matched low-z sample are slightly lower than for the same bins of the high-z sample (as shown by the difference in sSFR in Fig. 12). In contrast to the other matched samples, the ionization parameters of the sSFR-matched low- and high-z-matched samples are consistent within 1σ uncertainties (bottom panels, Fig. 11).

The difference between the ionization parameters of the matched samples is mostly independent of the diagnostic method used. For most of the matched samples, the two different diagnostics give the same offset between the ionization parameter and metallicity of the low versus high-z bins. We find only one instance for the stacked samples where the ionization parameter predicted by the KK04 diagnostic appears significantly greater than that inferred from IZI, the lowest sSFR bin of the high-z sample (Figs 11 and 12). We note that the discrepancy is likely to result from the difference in assumed ISM pressures. The KK04 diagnostic, which is based on a lower pressure, is ascribing the emission-line properties to a higher ionization parameter than IZI, which uses a higher model pressure.

We find differences of up to 0.17 dex between the ionization parameters inferred for the stacked samples via the two diagnostics. However, there does not appear to exist a systematic offset for the stacked samples. For the M_*-matched and SFR-matched, low-z samples the ionization parameters inferred via the KK04 diagnostic are $\sim$0.05 dex higher than inferred via IZI, whereas for the sSFR-matched, low-z sample the ionization parameters inferred via the KK04 diagnostic are 0.05 dex lower.

We test the difference between the ionization parameters inferred via the two diagnostics using the 136 H II regions from van Zee et al. (1998) with which we also investigate differences in the metallicity.
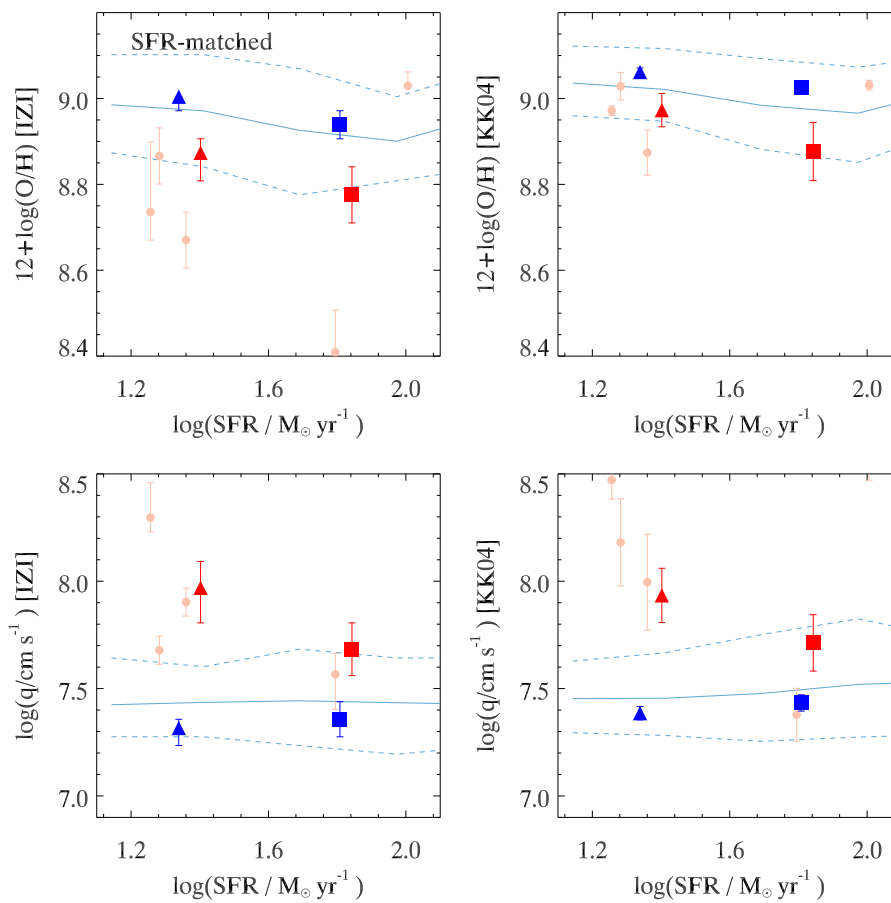
Figure 10. Metallicity and ionization parameter as a function of SFR for the SFR-matched low-z (blue filled symbols) and high-z (red filled symbols) samples. The subset of z 1.5 galaxies for which q and Z could be inferred individually is shown for comparison (pink filled symbols). Left column: results from the IZI diagnostic. Right column: results based on the KK04 diagnostic. The symbols for the binned and stacked samples are consistent with the second row in Fig. 2. The mean metallicity and ionization parameter (solid, light blue line), 16th and 84th percentiles (dashed light blue line) of the SFR-matched, SDSS sample derived via IZI (left-hand panels) and the KK04 diagnostic (right-hand panels) are shown as a function of SFR for comparison.

We use the log $P/k = 5$ pressure grid and applying the same set of emission lines used in the KK04 diagnostic when using IZI. Applying the same criteria, we find that the KK04 diagnostic predicts 0.07 dex higher ionization parameters, on average, than IZI with a dispersion about the mean of 0.08 dex, which is within the errors of the models (0.1 dex). If we instead use the set of five lines applied to our stacked samples, we find a mean offset of 0.09 dex with a 0.1 dex dispersion. The additional use of the total [S II]$\lambda\lambda$6717, 6713 flux resulted in a greater mean offset of 0.14 dex with a dispersion about the mean of 0.1 dex.

7 DISCUSSION

7.1 Validation of methods

We investigate how stacking spectra impacts the emission-line and ISM properties we derive for each sample. To assess the impact of stacking the high-z spectra, we compare the emission-line ratios derived via stacking to the individual ratios of the parent samples (Figs 6 to 8). Moreover, the stacked high-z bins exhibit [O III]/H β and [N II]/H α ratios that are consistent with the fit to the larger FMOS sample presented in Kashino et al. (2017; see the solid red line in Fig. 6).

We investigate the validity of our stacking method via the relationship between metallicity/ionization parameter and M_* in Fig. 13. The metallicities and ionization parameters inferred based on the stacked spectra are consistent with both the mean (solid grey) and median (solid black) values of the individual sample. Moreover, the relationship between the metallicity and M_* of our M_*-matched low-z sample is consistent with the MZ relation derived by Zahid et al. (2013; Fig. 13). The median metallicities of the M_*-matched sample (the solid black line in the upper right-hand panel of Fig. 13) are slightly lower than the MZ relation of Zahid et al. (2013), especially at the high-mass end. However, the MZ relation of Zahid et al. (2013) is based on a lower stellar mass range, indicated by the red dashed line in Fig. 13. The differences between our MZ relation and that of Zahid et al. (2013) are due to the difference in AGN selection criteria (Kewley et al. 2001 versus Kauffmann et al. 2003), the different stellar mass ranges, and the smaller size of our sample.

We further assess whether our stacking method results in any bias in the metallicity or ionization parameter within the low-z (SDSS) sample. As suggested by Kashino et al. (2017), simply taking the mean spectrum may yield emission line measurements that are weighted towards more luminous and therefore lower metallicity galaxies. Moreover, Telford et al. (2016) show that galaxies with higher sSFRs may have a larger fraction of light covered by
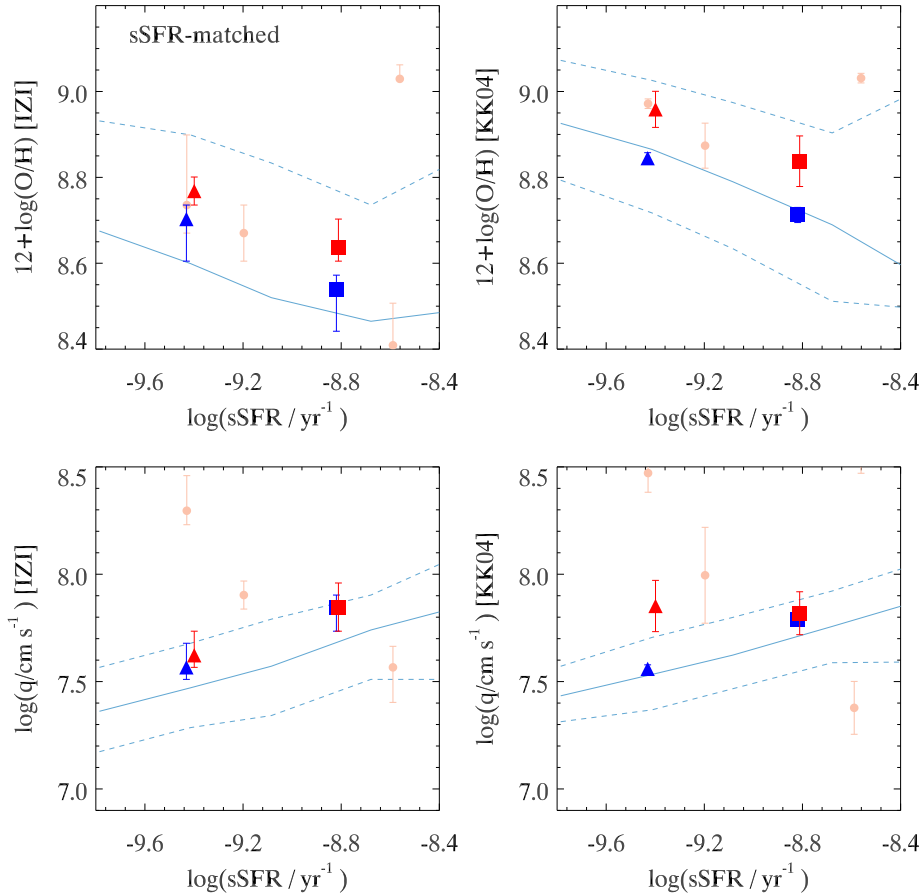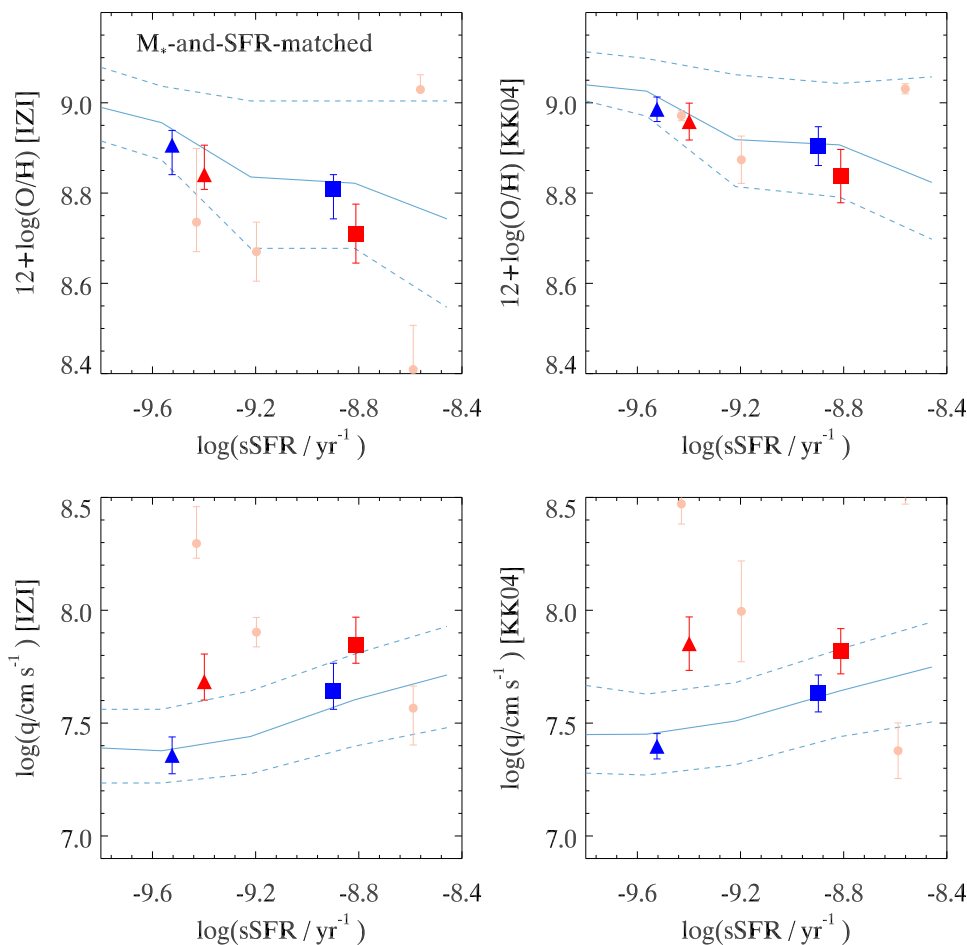
Figure 11. Metallicity and ionization parameter as a function of sSFR for the sSFR-matched low-*z* (blue filled symbols) and high-z (red filled symbols) samples. The subset of *z* 1.5 galaxies for which *q* and *Z* could be inferred individually is shown for comparison (pink filled symbols). Left column: results from the IZI diagnostic. Right column: results based on the KK04 diagnostic. The symbols for the binned and stacked samples are the same as in the right panel of the third row in Fig. 2. The mean metallicity and ionization parameter (solid, light blue line), 16th and 84th percentiles (dashed light blue line) of the sSFR-matched, SDSS sample derived via IZI (left-hand panels) and the KK04 diagnostic (right-hand panels) are shown as a function of sSFR for comparison.

the SDSS fibre and may therefore include lower metallicity regions of the galaxy. To test the extent to which our stacked emission-line measurements are weighted towards a more luminous subsample, we scale the spectra of the low-*z*, M_*-matched sample by the inverse of the peak H α flux prior to stacking. We find no significant difference between the Balmer decrements, metallicity, or ionization parameter derived via the simple averaging method versus the H α scaled method (Fig. 13). We therefore conclude that our stacking method does not significantly bias our results to either more luminous or low-metallicity galaxies. We also argue that the variation in aperture covering fractions with sSFR do not bias our stacked results as the metallicities and ionization parameters inferred based on the two stacked bins of sSFR-matched low-*z* galaxies are consistent with the mean values inferred individually for the sample (blue line versus filled blue symbols in Fig. 11).

We note that the ISM properties discussed in this work represent global averages, which do not account for the dispersion amongst galaxies. Our emission-line spectra represent the luminosity-weighted integrated spectra of regions of ionized interstellar gas which fall within our aperture. We further smooth the effects by stacking these integrated spectra in bins of global galaxy properties. We thereby assume that the metallicities and ionization parameters derived for the galaxy samples are representative of the conditions within the most luminous star-forming regions. More-

over, our work does not attempt to take into account the effects of diffuse gas emission discussed in Sanders et al. (2017). Instead, the impact of diffuse gas on the diagnostic methods used here will be discussed in Poetrodjojo (in preparation).

We have modelled the emission from the galaxies within our sample as coming from 'ionization-bounded' H II regions, for which the size is determined by the ionization equilibrium between the production rate of hydrogen-ionizing photons and the hydrogen recombination rate. Outside the 'ionization-bounded' H II region the hydrogen gas is 99 per cent neutral. In the alternative, 'density-bounded', scenario, the size of the H II region is defined by the distance at which the ionizing photons run out of matter to ionize. For a 'density-bounded' H II region, the gas density is low enough that the stars may completely ionize the hydrogen in the gas cloud, leaving no neutral H I gas outside the H II region. Density-bounded H II regions may have significantly smaller [N II] and [O II] zones, resulting in larger [O III]/H β and [O III]/[O II] ratios than what would be observed for ionization-bounded H II regions (Brinchmann et al. 2008; Kewley et al. 2013b; Nakajima & Ouchi 2014). If our simulations are applied to density-bounded nebulae, the larger line ratios may be interpreted as greater ionization parameters. Both ionization- and density-bounded nebulae have been observed in the Local Group (Pellegrini et al. 2012). However, it is still unclear which scenario is

Figure 12. Metallicity and ionization parameter as a function of sSFR for the M_*-and-SFR-matched low-z (blue) and high-z (red) samples. The subset of z 1.5 galaxies for which q and Z could be inferred individually is shown for comparison (pink filled symbols). Left column: results from the IZI diagnostic. Right column: results based on the KK04 diagnostic. Note that the position of the high-z sample is the same as in Fig. 11. The symbols are the same as in the bottom row of Fig. 2. The mean metallicity and ionization parameter (solid, light blue line), 16th and 84th percentiles (dashed light blue line) of the M_*-and-SFR-matched, SDSS sample derived via IZI (left-hand panels) and the KK04 diagnostic (right-hand panels) are shown as a function of sSFR for comparison.

most typical in main-sequence star-forming galaxies, either locally or at high redshift.

7.2 The evolution of ionization parameter

Our results indicate that the ionization parameter evolves with the sSFR of galaxies. We find that there is an evolution in the ionization parameter for main-sequence galaxies, from $z \sim 0.1$ to $z \sim 1.5$. However, once the differences in sSFR (from the evolution of the main sequence) are accounted for we find little evolution in the ionization parameter. Samples with consistent, high sSFRs exhibit equivalent, average ionization parameters. In contrast, samples of low-z galaxies for which only the M_* or SFR is equivalent to our high-z sample exhibit significantly lower average ionization parameters. Moreover, both the sSFR- and M_*-and-sSFR matched low-z samples appear to exhibit a positive correlation between the average ionization parameter and sSFR (i.e. the solid blue lines in Figs 11 and 12).

To validate the results of the stacked analysis and investigate the dependence of the ionization parameter on metallicity, M_*, and sSFR we determine the metallicity and ionization parameter individually for each galaxy in the low-z star-forming catalogue. We

derive the metallicity and ionization parameters via IZI using the strong emission lines, [O II]$\lambda\lambda3726$, 3729, H β, [O III]$\lambda5007$, H α, [N II]$\lambda6584$ and [S II]$\lambda\lambda6717$, 6731, and photoionization grids with an ISM pressure selected according to the [S II]$\lambda6717$/[S II]$\lambda6731$ ratio, as described in Section 5.1. We separate the low-z star-forming catalogue into bins of M_* and sSFR, each containing at least 20 galaxies, and show the mean metallicity and mean ionization parameter inferred via IZI as well as the number of galaxies per bin in Fig. 14. In each panel, we show the main sequence at $z \sim 0.1$ and $z \sim 0.3$ from Speagle et al. (2014; solid and dashed black lines, respectively). We note that the main trends are the same when using the KK04 diagnostic. However, the KK04 diagnostic shows a greater sensitivity of metallicity to sSFR than when we apply IZI and account for variations in pressure.

We find that the ionization parameter shows a strong variation with sSFR for the $z < 0.3$ sample of star-forming galaxies (Fig. 14), confirming the results from the matched samples. Within the $z < 0.3$ sample, the ionization parameter scales most strongly with the sSFR, and only shows a weak dependence on M_*, in that the highest ionization parameters are also found at the lowest values of M_*. In contrast to the ionization parameter, the metallicity scales most strongly with M_*, rather than sSFR (although the strength
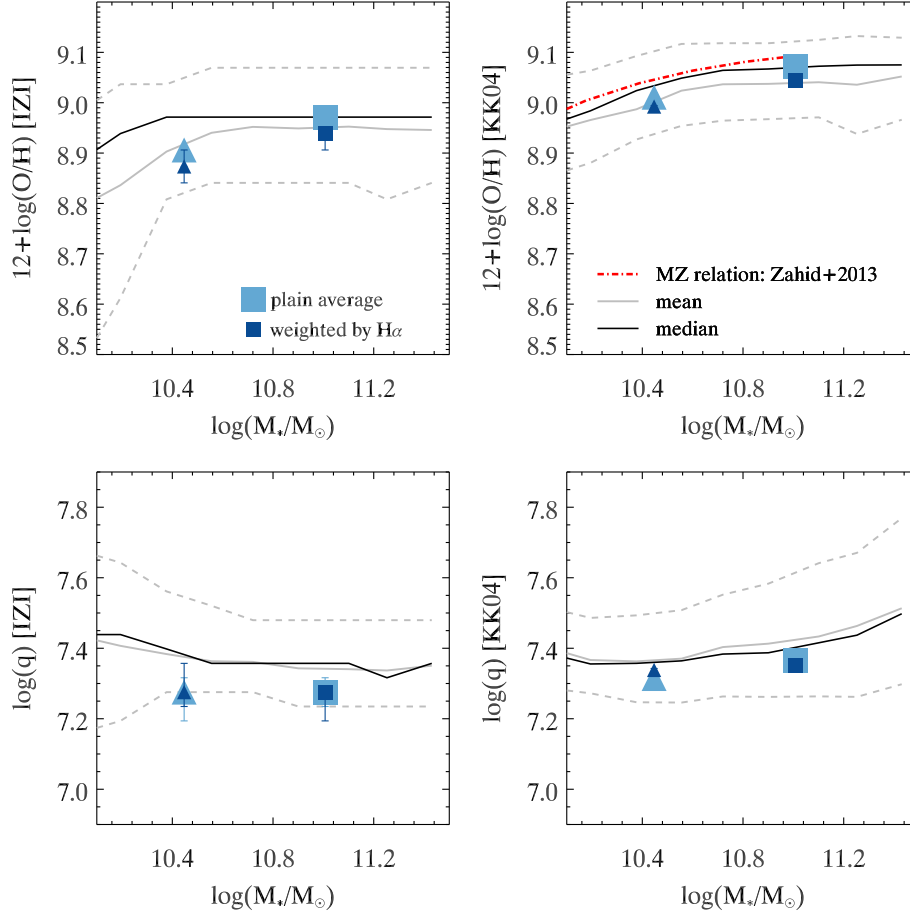
Figure 13. Metallicity (top row) and ionization parameter (bottom row) as a function of M_* for the low-z, M_*-matched sample. The mean and median of the sample, in bins if M_*, are shown by the grey and black lines, respectively. The dashed grey lines indicate the 16th and 84th percentiles. The results from two stacking methods are compared; the simple average method we have chosen (large light blue symbols) and weighting by the H α flux prior to stacking (small dark blue symbols). Left column: results based on the IZI diagnostic. Right column: results based on the KK04 diagnostic. The MZ relation of Zahid et al. (2013), based on the KK04 diagnostic, is shown for comparison (red dashed line, upper right-hand panel).
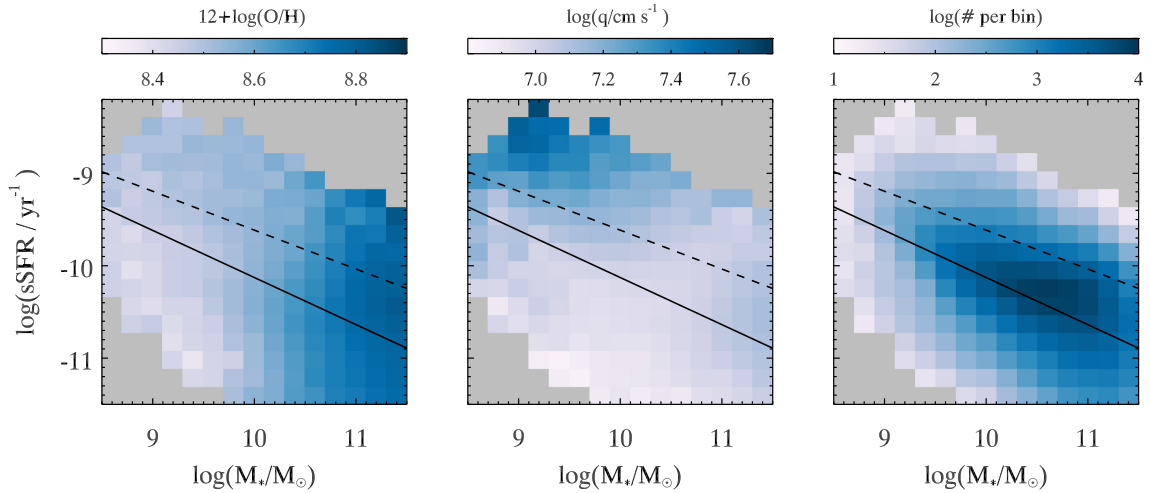
Figure 14. Mean metallicity (left) and ionization parameter (middle) as a function of M_* and sSFR for the full low-z star-forming catalogue. Each bin of M_* and sSFR contains at least 20 galaxies. The number of galaxies per bin is shown in the right hand panel. The metallicity and ionization parameter are based on IZI, using [O II], H β, [O III], H α, and [N II]. The main-sequence fits from Speagle et al. (2014) at $z \sim 0.1$ and $z \sim 0.3$ are shown by the solid and dashed black lines, respectively.

of the correlation with sSFR is sensitive to the diagnostic as well as the treatment of dust and aperture effects (Telford et al. 2016). Along the main sequence (black solid line), the mean metallicity increases significantly (by ∼0.6 dex) with M_*, whereas the ionization parameter shows no significant correlation with M_*.

Both our stacked samples and the low-z star-forming catalogue indicate that high-ionization parameters are not driven simply by low metallicities. Although the sSFR-matched, low-z sample has lower metallicities than the high-z sample, the ionization parameters of the two bins are consistent (see Fig. 11). Within the low-z star-forming catalogue the metallicity increases with M_* for sSFR $< 10^{-9.5}$ yr^{-1}, whereas the ionization parameter shows little variation. Bins with the lowest metallicities do not correspond to the highest ionization parameters. Nor does the mean ionization parameter follow the trend of increasing metallicity along the main sequence.

The dependence of the ionization parameter on sSFR, shown by our matched samples and within the low-z star-forming catalogue, is consistent with the correlations presented in Nakajima & Ouchi (2014), Kewley et al. (2015), Sanders et al. (2016), and Bian et al. (2016). Bian et al. (2016) compare two sets of local SDSS galaxies, selected according to their position on the BPT diagram. Those occupying positions consistent with main-sequence galaxies at $z \sim 2.3$, the 'local analogues', exhibited significantly greater ionization parameters and sSFRs than the local, main-sequence, star-forming galaxies. Both Nakajima & Ouchi (2014) and Sanders et al. (2016) show that the O_{32} ratio, a strong tracer of the ionization parameter, has a strong positive correlation with sSFR, a weak negative correlation with M_* and no clear correlation with SFR (as in Figs 9 to 12). Kewley et al. (2015) find a strong positive correlation between the ionization parameter and equivalent width of H β (EW(H β)). As discussed in Groves et al. (2012) and Kewley et al. (2015), the EW(H β) traces the age of the stellar population, where the value of EW(H β) increases with the relative proportion of young to old stars. The sSFR we measure (based on the H α luminosity) reflects the number of massive young (OB) stars formed in relation to the total number of stars and is therefore sensitive to the fraction of young to old stars, similar to the EW(H β) and EW(H α).

Based on our results, we argue that there exists an evolution in the ionization parameter with redshift that is driven by the evolving sSFR. The sensitivity of the ionization parameter to the sSFR may ensue from a relative increase in the hydrogen ionizing photon flux with respect to the gas density with greater sSFR. Because the hydrogen ionizing photons stem from massive young stars, the 'effective' ionization parameter of a galaxy will increase along with the relative proportion of young to old stars, or, the number of young stars per unit volume. Thus, the ionization parameter would be expected to correlate strongly with sSFR (and SFR density). An increase in SFR alone is not sufficient to result in an increased ionization parameter (Figs 10 and 14) because a higher SFR does not necessarily increase the mean hydrogen ionizing photon flux across an entire galaxy. Low-z galaxies with equivalent SFRs typically have higher M_* and lower sSFR (Fig. 2) than galaxies at $z \geq 1.5$, indicating a lower fraction of young-to-old stars and/or lower SFR densities.

We note that our interpretation differs from some of the previous high-z studies we have compared our work to (e.g. Nakajima & Ouchi 2014; Shapley et al. 2015; Sanders et al. 2016). Based on the results presented here, we argue that high-z, main-sequence galaxies exhibit higher ionization parameters than low-z, main-sequence galaxies. We attribute this difference in ionization parameters, and the observed difference in positions on some emission-line ratio diagrams, to the evolution of the sSFR. There are three main reasons

why we attribute the observed evolution of the ionization parameter to the sSFR, rather than metallicity or M_*. First, we use the metallicity as a second axis in our work, and thereby show clearly that even in cases where the metallicity of samples may be similar the ionization parameters are clearly offset. Secondly, we directly compare matched low- and high-z samples, allowing us to disentangle the importance of M_* and sSFR. Thirdly, we infer the metallicity and ionization parameter using combinations of emission-line ratios rather than using a single line ratio as a proxy, which could lead to misinterpretations regarding which ISM property is varying.

Although we have focused on the metallicity and ionization parameter, we also determine the electron density of our low-z matched samples via the [S II]λ6717/[S II]λ6731 ratio. We find no clear correlation between the electron densities and ionization parameters of our samples. Samples with the highest inferred electron densities (and ISM pressures) do not exhibit the highest ionization parameters and vice versa. Based on the mean (and median) [S II]λ6717/[S II]λ6731 ratios, the typical electron densities of the M_*-, SFR-, and sSFR-matched samples are ∼40, 120, and 60 cm^{-3}, respectively. Although the SFR-matched sample has the highest inferred electron density, the ionization parameters of the two SFR bins are $0.3-0.4$ dex lower than for the two bins of sSFR in the sSFR-matched sample. Moreover, the ionization parameters of the two M_* bins of the low-z, M_*-matched sample are only <0.1 dex lower than for the high SFR-matched sample, despite significantly higher electron densities. These results indicate that the ionization parameter does not scale directly with the electron density, and, cannot be used as a proxy to derive the electron density, as it was in Shirazi et al. (2014b).

We showed in Kaasinen et al. (2017) that samples of low- and high-z galaxies matched in SFR have similar electron densities. In contrast, samples matched in SFR alone do not exhibit the same ionization parameters. As discussed in Shirazi et al. (2014b), Nakajima & Ouchi (2014), Sanders et al. (2016), and others, one can derive a simple scaling relation,

$$q^3 \propto Q_0 n_e \epsilon^2, \tag{2}$$

between the ionizing photon production rate, Q_0, the electron density and the volume filling factor, ϵ, assuming the case of a Strömgren sphere in ionization equilibrium. The ionizing photon production rate, Q_0, scales directly with the SFR, for the H II region considered, and thus equation (2) implies that for a fixed value of SFR and electron density the ionization parameter scales as $q \propto \epsilon^{2/3}$. If this simple scaling relation extends to star-forming galaxies, then our results may imply that high sSFR galaxies have higher filling factors and therefore higher ionization parameters. However, volume filling factors have yet to be measured with sufficient accuracy either locally or at high redshift.

8 SUMMARY

We have investigated the evolution of the ionization parameter by comparing a set of main-sequence, star-forming galaxies at $z \sim 1.5$, derived from the FMOS-COSMOS and COSMOS-[O II] Surveys, to samples of star-forming galaxies at $z < 0.3$, taken from SDSS. To separate the effects of M_*, SFR, and sSFR on the evolution of the ionization parameter, we selected four 'matched' comparison samples at $z < 0.3$. The first sample contains galaxies with equivalent M_* to the galaxies in our $z \sim 1.5$ sample and is representative of main-sequence galaxies at $z \sim 0.1$, the majority of which have significantly lower SFRs than the $z \sim 1.5$ sample. The second sample is comprised of galaxies with the equivalent SFRs to the galaxies in

our $z \sim 1.5$ sample and is biased towards higher M_* than the $z \sim 1.5$ sample. The third local comparison sample is matched in sSFR, and has lower stellar masses and SFRs than our high-z sample. The final local comparison sample contains galaxies with similar M_* and SFR to the galaxies in our high-z sample.

In order to derive properties that are representative of the $z \sim 1.5$ sample, we rely on a stacked analysis of the matched samples. We bin each sample according to the property in which it is matched, such that the distribution of the properties being matched is consistent for each pair of $z < 0.3$ and $z \sim 1.5$ bins. We use the relative emission-line fluxes of the stacked spectra to diagnose the metallicity and ionization parameter via two diagnostic methods; the Bayesian inference algorithm IZI and the widely used KK04 diagnostic. We take into account the variation in ISM pressure of the samples being used when applying IZI by selecting photoionization models with ISM pressures inferred from the measured [S II]$\lambda 6717$/[S II]$\lambda 6731$ and [O II]$\lambda 3729$/[O II]$\lambda 3726$ ratios. Although the values of metallicity and ionization parameter are offset between the two diagnostic methods, the conclusions drawn from the two are equivalent.

Our main conclusions are as follows:

(i) The ionization parameter of main-sequence galaxies evolves by 0.4 dex from $z \sim 0.1$ to $z \sim 1.5$.

(ii) The ionization parameter evolves with the sSFR of star-forming galaxies. There is no evolution in the ionization parameter from $z \sim 0.1$ to $z \sim 1.5$ when the change in sSFR is taken into account.

(iii) The evolution of the ionization parameter is not the by-product of the evolution of the metallicity. The ionization parameters of galaxies at the same redshift vary by ~ 0.5 dex for constant metallicity. Moreover, the ionization parameter scales most strongly with sSFR, whereas the metallicity increases with M_*.

By matching samples we have shown that star-forming galaxies with equivalently high sSFRs have similar ionization parameters, regardless of the consistency of M_*, SFR, or metallicity. We put forward a simple physical explanation for the increase in ionization parameter with sSFR. The ionization parameter is defined as the ratio between the hydrogen ionizing photon flux and the number density of hydrogen atoms. A high ionization parameter may therefore result from a high relative proportion of young to old stars and/or a greater number of young stars per unit volume, both of which are observed as a high sSFR.

Much observational work remains to be undertaken to understand the effects of the ionization parameter and ISM pressure on the evolution of star-forming galaxies. With the launch of *James Webb Space Telescope*, it will become possible to greatly increase the number of galaxies with emission-line spectroscopy, allowing for more detailed, statistical studies of the metallicity, ionization parameter and ISM pressure at high redshift. However, contributions from diffuse gas emission can have a significant impact upon the ISM properties derived from strong emission lines. Spatially resolved studies of star-forming galaxies across different cosmic epochs (e.g. via integral field spectroscopy surveys) will help address this issue, yielding further insight into the evolution of metallicity, ISM pressure and the ionization parameter as well as the effects of applying region diagnostics to entire galaxies.

REFERENCES

Abazajian K. N. et al., 2009, ApJS, 182, 543
Arnouts S., Ilbert O., 2011, Astrophysics Source Code Library , record ascl:1108.009
Asplund M., Grevesse N., Sauval A. J., Scott P., 2009, ARA&A, 47, 481
Baldwin J. A., Phillips M. M., Terlevich R., 1981, PASJ, 93, 5
Bian F., Kewley L. J., Dopita M. A., Juneau S., 2016, ApJ, 822, 62
Bian F. et al., 2010, ApJ, 725, 1877
Blanc G. A., Kewley L., Vogt F. P. A., Dopita M. A., 2015, ApJ, 798, 99
Brinchmann J., Charlot S., White S. D. M., Tremonti C., Kauffmann G., Heckman T., Brinkmann J., 2004, MNRAS, 351, 1151
Brinchmann J., Pettini M., Charlot S., 2008, MNRAS, 385, 769
Bruzual G., Charlot S., 2003, MNRAS, 344, 1000
Calvi V., Stiavelli M., Bradley L., Pizzella A., Kim S., 2014, ApJ, 796, 102
Cardelli J. A., Clayton G. C., Mathis J. S., 1989, ApJ, 345, 245
Cooper M. C., Newman J. A., Davis M., Finkbeiner D. P., Gerke B. F., 2012, Astrophysics Source Code Library , record ascl:1203.003
Daddi E. et al., 2007, ApJ, 670, 156
Dickey C. M. et al., 2016, ApJ, 828, L11
Dopita M. A., Sutherland R. S., 2003, Astrophysics of the Diffuse Universe. Springer-Verlag, Berlin, New York
Dopita M. A., Sutherland R. S., Nicholls D. C., Kewley L. J., Vogt F. P. A., 2013, ApJS, 208, 10
Dopita M. A. et al., 2006a, ApJS, 167, 177
Dopita M. A. et al., 2006b, ApJ, 647, 244
Elbaz D. et al., 2011, A&A, 533, A119
Elmegreen B. G., Elmegreen D. M., 2005, ApJ, 627, 632
Erb D. K., Steidel C. C., Shapley A. E., Pettini M., Reddy N. A., Adelberger K. L., 2006, ApJ, 646, 107
Foster C. et al., 2012, A&A, 547, A79
Förster Schreiber N. M. et al., 2006, ApJ, 645, 1062
Geller M. J., Hwang H. S., Fabricant D. G., Kurtz M. J., Dell'Antonio I. P., Zahid H. J., 2014, ApJS, 213, 35
Genzel R. et al., 2008, ApJ, 687, 59
Groves B., Brinchmann J., Walcher C. J., 2012, MNRAS, 419, 1402
Groves B. A., Heckman T. M., Kauffmann G., 2006, MNRAS, 371, 1559
Hainline K. N., Shapley A. E., Kornei K. A., Pettini M., Buckley-Geer E., Allam S. S., Tucker D. L., 2009, ApJ, 701, 52
Hao C.-N., Kennicutt R. C., Johnson B. D., Calzetti D., Dale D. A., Moustakas J., 2011, ApJ, 741, 124
Hayashi M. et al., 2015, PASJ, 67, 80
Holden B. P. et al., 2016, ApJ, 820, 73
Ilbert O. et al., 2013, A&A, 556, A55

Ilbert O. et al., 2015, A&A, 579, A2

Iwamuro F. et al., 2012, PASJ, 64, 59

Jenkins E. B., 2013, Proc. Sci., Depletions of Elements from the Gas Phase: A Guide on Dust Compositions. SISSA, Trieste, PoS(LCDU2013)005

Juneau S. et al., 2014, ApJ, 788, 88

Kaasinen M., Bian F., Groves B., Kewley L. J., Gupta A., 2017, MNRAS, 465, 3220

Kashino D. et al., 2013, ApJ, 777, L8

Kashino D. et al., 2017, ApJ, 835, 88

Kauffmann G. et al., 2003, MNRAS, 346, 1055

Kewley L. J., Dopita M. A., 2002, ApJS, 142, 35

Kewley L. J., Dopita M. A., Leitherer C., Davé R., Yuan T., Allen M., Groves B., Sutherland R., 2013b, ApJ, 774, 100

Kewley L. J., Dopita M. A., Sutherland R. S., Heisler C. A., Trevena J., 2001, ApJ, 556, 121

Kewley L. J., Ellison S. L., 2008, ApJ, 681, 1183

Kewley L. J., Jansen R. A., Geller M. J., 2005, PASP, 117, 227

Kewley L. J., Maier C., Yabe K., Ohta K., Akiyama M., Dopita M. A., Yuan T., 2013a, ApJ, 774, L10

Kewley L. J., Zahid H. J., Geller M. J., Dopita M. A., Hwang H. S., Fabricant D., 2015, ApJ, 812, L20

Kobulnicky H. A., Kewley L. J., 2004, ApJ, 617, 240

Kramida A., Ralchenko Yu., Reader J., NIST ASD Team, 2015, NIST Atomic Spectra Database Lines Data, (version 5.3). National Institute of Standards and Technology, Gaithersburg, MD, Available at: http://physics.nist.gov/asd

Laigle C. et al., 2016, ApJS, 224, 24

Levesque E. M., Kewley L. J., Larson K. L., 2010, AJ, 139, 712

Liu X., Shapley A. E., Coil A. L., Brinchmann J., Ma C.-P., 2008, ApJ, 678, 758

Madau P., Dickinson M., 2014, ARA&A, 52, 415

Mancini C. et al., 2011, ApJ, 743, 86

Mannucci F., Cresci G., Maiolino R., Marconi A., Gnerucci A., 2010, MNRAS, 408, 2115

Masters D., Faisst A., Capak P., 2016, ApJ, 828, 18

Masters D. et al., 2014, ApJ, 785, 153

McCracken H. J. et al., 2012, A&A, 544, A156

Murphy E. J. et al., 2011, ApJ, 737, 67

Nakajima K., Ouchi M., 2014, MNRAS, 442, 900

Newman J. A. et al., 2013, ApJS, 208, 5

Newman S. F. et al., 2014, ApJ, 781, 21

Nicholls D. C., Dopita M. A., Sutherland R. S., Kewley L. J., Palay E., 2013, ApJS, 207, 21

Nicholls D. C., Sutherland R. S., Dopita M. A., Kewley L. J., Groves B. A., 2017, MNRAS, 466, 4403

Osterbrock D. E., Ferland G. J., 2006, Astrophysics of Gaseous Nebulae and Active Galactic Nuclei, 2nd edn. University Science Books, Mill Valley, CA

Pellegrini E. W., Oey M. S., Winkler P. F., Points S. D., Smith R. C., Jaskot A. E., Zastrow J., 2012, ApJ, 755, 40

Salpeter E. E., 1955, ApJ, 121, 161

Sanders R. L., Shapley A. E., Zhang K., Yan R., 2017, ApJ, 850, 136

Sanders R. L. et al., 2016, ApJ, 816, 23

Shapley A. E. et al., 2015, ApJ, 801, 88

Shirazi M., Brinchmann J., Rahmati A., 2014b, ApJ, 787, 120

Shirazi M., Vegetti S., Nesvadba N., Allam S., Brinchmann J., Tucker D., 2014a, MNRAS, 440, 2201

Silverman J. D. et al., 2015, ApJS, 220, 12

Speagle J. S., Steinhardt C. L., Capak P. L., Silverman J. D., 2014, ApJS, 214, 15

Steidel C. C. et al., 2014, ApJ, 795, 165

Stoughton C. et al., 2002, AJ, 123, 485

Tacconi L. J. et al., 2010, Nature, 463, 781

Tachiev G., Fischer C. F., 2001, Can. J. Phys., 79, 955

Telford O. G., Dalcanton J. J., Skillman E. D., Conroy C., 2016, ApJ, 827, 35

Tremonti C. A. et al., 2004, ApJ, 613, 898

Trujillo I. et al., 2007, Astrophys. Space Sci. Proc., 3, 481

Trump J. R. et al., 2011, ApJ, 743, 144

van der Wel A. et al., 2014, ApJ, 788, 28

van Zee L., Salzer J. J., Haynes M. P., O'Donoghue A. A., Balonek T. J., 1998, AJ, 116, 2805

Vogt F. P. A., Dopita M. A., Kewley L. J., Sutherland R. S., Scharwächter J., Basurah H. M., Ali A., Amer M. A., 2014, ApJ, 793, 127

York D. G. et al., 2000, AJ, 120, 1579

Zahid H. J., Dima G. I., Kewley L. J., Erb D. K., Davé R., 2012, ApJ, 757, 54

Zahid H. J., Geller M. J., Kewley L. J., Hwang H. S., Fabricant D. G., Kurtz M. J., 2013, ApJ, 771, L19

Zahid H. J., Dima G. I., Kudritzki R.-P., Kewley L. J., Geller M. J., Hwang H. S., Silverman J. D., Kashino D., 2014a, ApJ, 791, 130

Zahid H. J. et al., 2014b, ApJ, 792, 75

This paper has been typeset from a TEX/LATEX file prepared by the author.